Supplementary Information for
Robust Fourier ptychographic structured illumination microscopy (FP-SIM) using only 3 patterns

Jiaming Qian[1,2,3], Ying Bi[1,2,3], Jixiang Zhou[1,2,3], Yu Cao[1,2,3], Yefeng Shu[1,2,3], Yongtao Liu[1,2,3], Haigang Ma[1,2,3], Hongjun Wu[1,2,3], Qian Chen[3,], and Chao Zuo[1,2,3,*]**

[1]Smart Computational Imaging (SCI) Laboratory, Nanjing University of Science and Technology, Nanjing, Jiangsu Province 210094, China
[2]Smart Computational Imaging Research Institute (SCIRI) of Nanjing University of Science and Technology, Nanjing, Jiangsu Province 210094, China
[3]Jiangsu Key Laboratory of Spectral Imaging & Intelligent Sense, Nanjing University of Science and Technology, Nanjing, Jiangsu Province 210094, China
[*]zuochao@njust.edu.cn
[**]chenqian@njust.edu.cn

ABSTRACT

This document provides supplementary information for "Robust Fourier ptychographic structured illumination microscopy (FP-SIM) using only 3 patterns". We discuss in detail the principles of FP-SIM, and present more comparative simulations and experiments. In addition, we provide an introduction to the open-source MATLAB code of FP-SIM and associated datasets, as well as the corresponding user guide and demo results.

Contents

S1. Forward model of structured illumination microscopy

Structured illumination microscopy (SIM) has become a widely available technique for insight into biomedical research, benefiting from fast imaging speed and low phototoxicity and bleaching properties[1]. Using spatially structured illumination patterns, SIM doubles the lateral resolution (∼200 nm) of the conventional microscope by modulating the high-frequency information of the sample into the system detection passband.

In a typical linear fluorescence microscopy system, the observed image is the convolution of the emitted fluorescence intensity (which is proportional to the excitation intensity) of the sample and the point spread function (PSF) of the microscopy, which can be written as:

$$D(\mathbf{r}) = [I(\mathbf{r}) \cdot S(\mathbf{r})] \odot H(\mathbf{r}) \tag{S1}$$

where $\mathbf{r}$ represents the image spatial coordinate, S denotes the sample signal, I refers to the excitation intensity, H is PSF, and $\odot$ represents convolution operation. For SIM, the illumination pattern I satisfies the sinusoidal distribution, then $D(\mathbf{r})$ can be rewritten as:

$$D(\mathbf{r}) = \{S(\mathbf{r})[1 + m\cos(2\pi \mathbf{k}_{ex}\mathbf{r})]\} \odot H(\mathbf{r}) \tag{S2}$$

where m and $\mathbf{k}_{ex}$ represent the illumination modulation depth and spatial frequency / wave vector, separately. The Fourier spectrum of Eq. S2 can be expressed as:

$$\tilde{D}(\mathbf{k}) = \tilde{S}_0(\mathbf{k})O(\mathbf{k}) + \frac{m}{2}\tilde{S}_1(\mathbf{k} - \mathbf{k}_{ex})O(k) + \frac{m}{2}\tilde{S}_{-1}(\mathbf{k} + \mathbf{k}_{ex})O(\mathbf{k}) \tag{S3}$$

where $\mathbf{k}$ represents the frequency coordinate, $\sim$ denotes the Fourier transform of the original object, subscripts 0 and ± 1 are the orders of different spectrum components, and O is the optical transfer function (OTF), which is the Fourier transform of PSF. It is easy to see from Eq. S3 that the ± 1-order spectrums carry the sample information from its original position with $\pm \mathbf{k}ex$ frequency. In other words, sinusoidally structured illumination modulation enables the image spectrum to contain super-resolution information beyond the diffraction limit, the extension of which is determined by the illumination wave vector. Since the illumination pattern is also limited by the system OTF, $\mathbf{k}ex$ is maximally close to the original cutoff frequency, meaning that SIM can double the lateral resolution. In order to recover super-resolution information from the original illumination image mixed with wide-field signals and high-frequency signals outside the diffraction limit, it is necessary to separate the three (0- and ± 1-order) spectrum components and reorganize them to their correct positions.

S2. Conventional 9-frame SIM reconstruction algorithm

Demodulating high-frequency information from the original SIM image is a highly ill-posed inverse problem, and the classical solution is to introduce at least two additional phase-shifting images and solve for the three spectral components by linearly combining between raw SIM observations. Typically, the three-step phase-shifting illumination images D_n ($n = 1,2,3$) with phase shift $\varphi = 2\pi/3$ can be represented as (Fig. S1b and S1c):

$$D_n(\mathbf{r}) = \{S(\mathbf{r})[1+m\cos(2\pi\mathbf{k}_{ex}+(n-1)\varphi+\varphi_0)]\}\odot H(\mathbf{r}) \tag{S4}$$

where φ_0 represents the initial phase. Fig. S1a illustrates the optical setup for generating sinusoidal structured illumination, where the ±1-order diffraction light generated by the incident on a spatial light modulator (SLM) displaying a high-frequency grating pattern interferes to produce an interference fringe pattern (for a detailed description of the SIM system see Section S11). The Fourier spectrums of Eq. S4 can be expressed as (Fig. S1d):

$$\tilde{D}_n(\mathbf{k}) = \frac{m}{2}O(\mathbf{k})\tilde{S}_1(\mathbf{k}-\mathbf{k}_{ex})e^{j[2\pi(n-1)/3+\varphi_0]} + O(\mathbf{k})\tilde{S}_0(\mathbf{k}) + \frac{m}{2}O(\mathbf{k})\tilde{S}_{-1}(\mathbf{k}+\mathbf{k}_{ex})e^{-j[2\pi(n-1)/3+\varphi_0]} \tag{S5}$$

Through the known phase shift φ, the 0- and ±1-order spectrum components can then be separated by:

$$\begin{bmatrix} O(\mathbf{k})\tilde{S}_0(\mathbf{k}) \\ mO(\mathbf{k})\tilde{S}_{-1}(\mathbf{k}+\mathbf{k}_e x)e^{-j\varphi_0} \\ mO(\mathbf{k})\tilde{S}_1(\mathbf{k}-\mathbf{k}_e x)e^{j\varphi_0} \end{bmatrix} = \begin{bmatrix} 1 & \frac{1}{2} & \frac{1}{2} \\ 1 & \frac{1}{2}e^{-j\frac{2\pi}{3}} & \frac{1}{2}e^{j\frac{2\pi}{3}} \\ 1 & \frac{1}{2}e^{-j\frac{4\pi}{3}} & \frac{1}{2}e^{j\frac{4\pi}{3}} \end{bmatrix}^{-1} \begin{bmatrix} \tilde{D}_1(\mathbf{k}) \\ \tilde{D}_2(\mathbf{k}) \\ \tilde{D}_3(\mathbf{k}) \end{bmatrix} \tag{S6}$$

For simplicity, we write $C_0 = O(\mathbf{k})\tilde{S}_0(\mathbf{k})$, $C_1 = mO(\mathbf{k})\tilde{S}_1(\mathbf{k}-\mathbf{k}_{ex})e^{j\varphi_0}$ and $C_{-1} = mO(k)\tilde{S}_{-1}(\mathbf{k}+\mathbf{k}_{ex})e^{-j\varphi_0}$, where C_0 and $C_{\pm 1}$ represent the wide-field and high-frequency information, respectively (Fig. S1e). However, the separated spectrum components carry the modulation depth m and initial phase $e^{\pm j\varphi_0}$ associated with the experimental environment, which will cause severe artifacts in the subsequent reconstruction if not compensated[2]. Moreover, the wave vector $\mathbf{k}ex$ required for the spectrum reorganization is also environment-sensitive and needs to be estimated a posteriori from the captured raw images. The iterative cross-correlation method (COR) proposed by Gustafsson *et al.*[3] is one of the most widely used parameter estimation approaches, which determines the wave vector with sub-pixel accuracy in the form of real-space phase gradients, and on this basis calculates the initial phase and modulation by complex linear regression. Taking the 1-order spectrum C_1 as an example, its spectrum peak can be easily located and C_1 can be frequency shifted by the integer-pixel wave vector (the distance from the localized spectrum peak to the image center, which can be written as $\mathbf{k}_{int}$. Note that $\mathbf{k}_{ex}$ can be decomposed into $\mathbf{k}_{int}$ and $\mathbf{k}_{sub}$, where $\mathbf{k}_{sub}$ denotes the residual sub-pixel component). The shifted C_1 can be rewritten as $mO(\mathbf{k}+\mathbf{k}_{int})\tilde{S}_1(\mathbf{k}-\mathbf{k}_{sub})e^{j\varphi_0}$. Then we remove the OTF terms of C_0 and C_1:

$$C_0' = C_0\frac{O^*(\mathbf{k})}{|O(\mathbf{k})|^2} = \tilde{S}_0(\mathbf{k}) \tag{S7}$$

$$C_1' = C_1\frac{O^*(\mathbf{k}+\mathbf{k}_{int})}{|O(\mathbf{k}+\mathbf{k}_{int})|^2} = m\tilde{S}_1(\mathbf{k}-\mathbf{k}_{sub})e^{j\phi_0} \tag{S8}$$

where superscript * represents the complex conjugate, and the system OTF can be obtained by calibration or numerical simulation. In fact, C_0' and C_1' are inherently and highly correlated, and their correlation value will reach its maximum at a shift of $\mathbf{k}_{sub}$. Such maximum correlation can be obtained by iterative search in progressively finer steps around the peak of C_1':

$$Cor(\mathbf{k}'_{sub}) = \frac{\sum_{\mathbf{k}} m\tilde{S}_0^*(\mathbf{k})\tilde{S}_1(\mathbf{k}-\mathbf{k}_{sub}+\mathbf{k}'_{sub})e^{j\phi_0}}{\sum_{\mathbf{k}}|\tilde{S}_0(\mathbf{k})|^2} \tag{S9}$$

$$\mathbf{k}_{sub} = \underset{\mathbf{k}'_{sub}\in[-1,1]}{argmax}\; Cor(\mathbf{k}'_{sub}) \tag{S10}$$

where $\mathbf{k}'_{sub}$ represents the varying sub-pixel distance, Cor denotes the normalized cross-correlation value of C_0' and C_1' at $\mathbf{k}'_{sub}$, and $argmax$ is the operation to determine the maximum value. According to Fourier frequency shift characteristics, the sub-pixel frequency shifts can be conveniently implemented by phase shifting in real space. Then, Eq. S9 can be transformed into:

$$Cor(\mathbf{k}'_{sub}) = \frac{\sum_{\mathbf{k}} mS_0^*(\mathbf{r})S_1(\mathbf{r})e^{(j\phi_0+\mathbf{k}_{sub}\mathbf{r}-\mathbf{k}'_{sub}\mathbf{r})}}{\sum_{\mathbf{r}}|S_0(\mathbf{r})|^2} \tag{S11}$$

After accurately determining $\mathbf{k}_{sub}$ and sub-pixel shifting C_1' to the correct position, the initial phase and modulation depth can be obtained by complex linear regression:

$$\varphi_0 = angle(\frac{\sum_{\mathbf{k}} mS_0^*(r)S_1(\mathbf{r})e^{j\varphi_0}}{\sum_{\mathbf{k}}|S_0(\mathbf{r})|^2}) \tag{S12}$$

$$m_0 = \left|\frac{\sum_{\mathbf{k}} mS_0^*(\mathbf{r})S_1(\mathbf{r})e^{j\varphi_0}}{\sum_{\mathbf{k}}|S_0(\mathbf{r})|^2}\right| \tag{S13}$$

where $angle()$ is the operation that returns the phase. After estimating the initial phase, wave vector and modulation depth, the three spectrum components can be precisely separated and reorganized (Fig. S1f). For isotropic super-resolution, the same operation is performed on two other sets of SIM raw images with fringe orientations rotating by 120 degrees (Fig. S1g). Therefore, the conventional SIM reconstruction methods require at least 9 original illumination images to complete the super-resolution reconstruction. Finally, the Wiener filter is used to weighted average the different spectrum components, and inverse Fourier transform is conducted to obtain the super-resolution image:

$$S = \mathscr{F}^{-1}\frac{\sum_{i,q} O(\mathbf{k}+q\mathbf{k}_{i,ex})\tilde{S}_{i,q}(\mathbf{k})O^*(\mathbf{k}+q\mathbf{k}_{i,ex})}{\sum_{i,q}|O(\mathbf{k}+q\mathbf{k}_{i,ex})|^2+w^2}A(\mathbf{k})) \tag{S14}$$

where $\mathscr{F}^{-1}$ denotes the inverse Fourier transform, the subscript i represents the different directions of the interference fringes / illumination patterns ($i = 1,2,3$), the subscript q is the order of the separated spectrum ($q = -1,0,1$), w is Wiener constant dependent on experience, and A is an apodization function to suppress high-frequency artifacts.

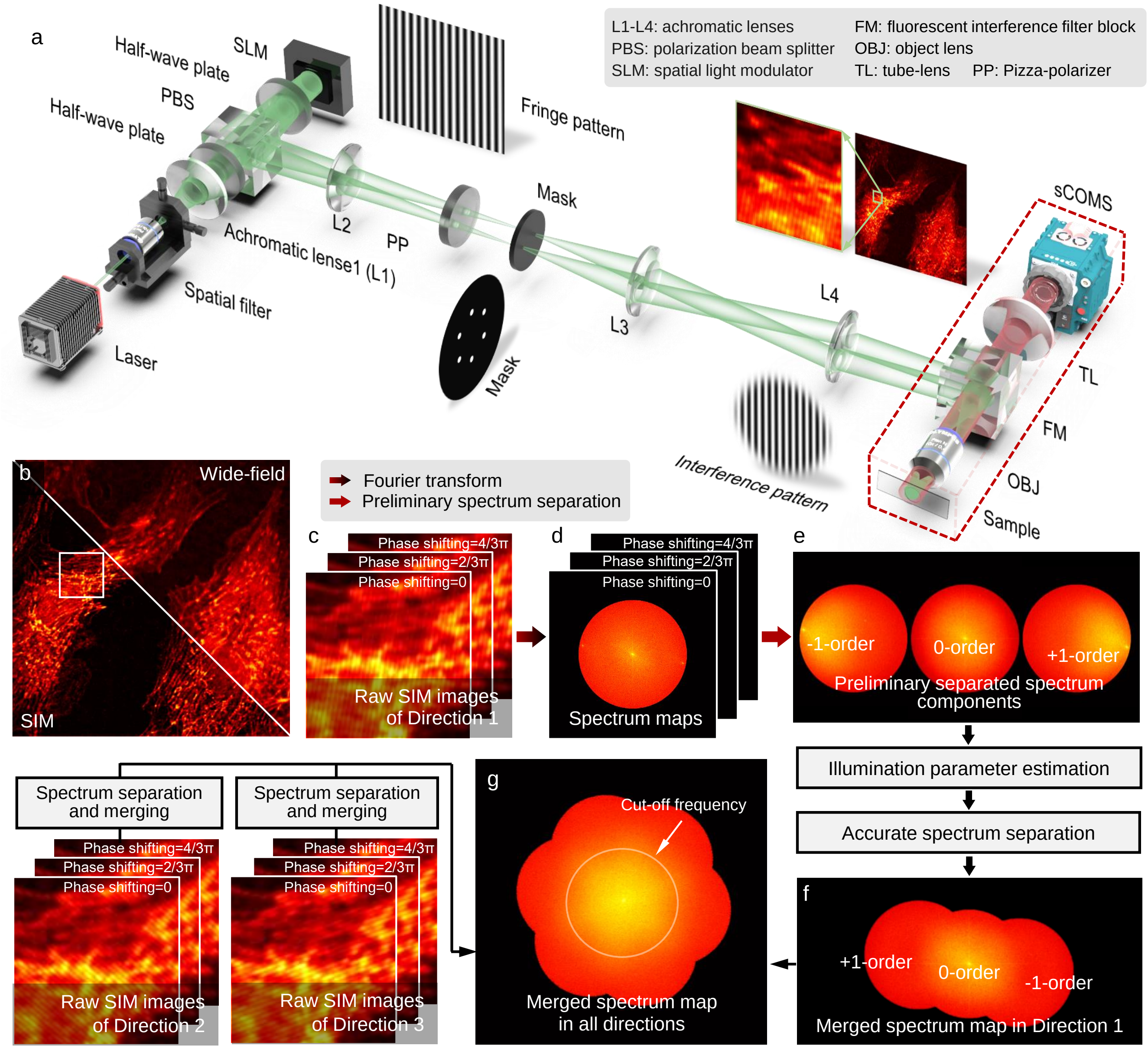

Figure S1. The principle of conventional 9-frame SIM reconstruction algorithm. a Schematic diagram of the optical path of an interferometric SIM system, where the ±1-order diffraction light generated by the incident on a spatial light modulator (SLM) displaying a high-frequency grating pattern interferes to produce an interference fringe pattern. **b** Comparison between the wide-field image and the super-resolution image. **c** Raw SIM image of a certain illumination orientation from the boxed region in **b**. **d** The spectrum map of **c**. **e** Initially separated spectrum components. **f** Merged spectrum in a single illumination direction. **g** Merged spectrum in three illumination directions

S3. 3-frame Fourier ptychographic SIM reconstruction algorithm

Fourier ptychographic microscopy

Fourier ptychographic microscopy (FPM) is a wide-field, high-resolution computational microscopy technology[4], which can iteratively stitch together numerous large field-of-view, low-resolution images obtained by illuminating the sample with plane waves at variable angles to produce a high-resolution target image in Fourier space:

$$SP^{k+1}(\mathbf{k}) = \sum_{l} \{Pty[SP_l^k(\mathbf{k}), sp_l(\mathbf{r})] - SP_l^k(\mathbf{k})\} + SP^k(\mathbf{k}) \tag{S15}$$

$$Pty[SP_l^k(\mathbf{k}), sp_l(\mathbf{r})] = \mathscr{F}\{\sqrt{sp_l(\mathbf{r})}\frac{\mathscr{F}^{-1}[SP_l^k(\mathbf{k})]}{|\mathscr{F}^{-1}[SP_l^k(\mathbf{k})]|}\} \tag{S16}$$

where SP represents the high-resolution target in FPM, k denotes the iteration times, the subscript l is the l-th illumination angle, SP_l represents a small subregion of SP corresponding to illumination angle l, sp_l is the low-resolution measurement obtained under illumination angle l, and Pty denotes the operation of replacing the amplitude of the target with sp_l. The initial guess of SP is usually the sample image (with the phase field set to zero) acquired by the plane wave illumination at positive incidence. The iteration is repeated until SP converges.

Fourier ptychographic structured illumination microscopy

FPM is essentially an optimization process to seek a high-resolution complex field solution of the object with the constraint of multiple low-resolution images captured. We directly apply the idea of FPM to SIM. Different from FPM which recovers both amplitude and phase, SIM mainly focuses on amplitude / intensity information. Therefore, the operation of Pty is discarded and the optimization procedure of Fourier ptychographic SIM (FP-SIM) is written as follows with reference to Eq. S15:

$$S^{k+1}(\mathbf{r}) = Dec\sum_{i} [D_i(\mathbf{r})/I_i(\mathbf{r}) - H(\mathbf{r}) \odot S^k(\mathbf{r})] + S^k(\mathbf{r}) \tag{S17}$$

where S represents the high-resolution target in SIM, *i.e.*, the sample signal, the subscript i denotes the i-th illumination orientation, D_i is the low-resolution measurement obtained under illumination orientation i, *i.e.*, the original SIM image, I_i represents the illumination pattern corresponding to illumination orientation i, and Dec denotes the deconvolution operation for weighted averaging of the different spectrum components. Similar to the operation $Pty[SP_l^k(\mathbf{k}), sp_l(\mathbf{r})] - SP_l^k(\mathbf{k})$ in Eq. S15 in order to recover the high-frequency information in a certain subregion of SP, the operation $D_i(\mathbf{r})/I_i(\mathbf{r}) - H(\mathbf{r}) \odot S^k(\mathbf{r})$ implements the extension of the high-frequency component in the mixing spectrums, as shown in Fig. S7. Compared to conventional 9-frame SIM reconstruction algorithm (Fig. S1), Fourier ptychographic SIM reconstruction requires only one original measurement per illumination orientation, and the imaging efficiency is improved by a factor of three while the photodamage is reduced by a factor of three. The initial estimation and iteration termination condition for Eq. S17 are discussed in Sections S7-S9.

S4. Super-resolution performance discussion of Fourier ptychographic structured illumination microscopy

Unlike in FPM where each sub-aperture image is acquired separately, for SIM, images of different sub-apertures (*i.e.*, images corresponding to each spectrum component) are mixed. How to separate and expand these sub-aperture spectrums is the key to achieving super-resolution reconstruction. In conventional 9-frame SIM, spectrum separation is accomplished by acquiring additional phase-shifting images and linearly combining them through Eq. S6, based on which spectrum recombination is then achieved by hard-to-obtain illumination parameters. In this process, the step-by-step spectrum separation and recombination will pass the error to the next step respectively, making it difficult to obtain the optimal solution. In FP-SIM, spectrum extension is realized by the illumination inversion operation of $D_i(\mathbf{r})/I_i(\mathbf{r})$. As illustrated in Figs. S2a and S2b, such a simple operation in the real-space domain effectively shifts the ±1-order spectrum components and expands the spectrum support domain, which is more evident in the spectrum difference image as shown in Fig. S2c. It should be noted that since the acquired illumination patterns are not exactly consistent with the actual ones, accurate super-resolution information cannot be obtained by one illumination inversion. With the data redundancy provided by a certain overlap rate between different spectrum components, performing the above operations jointly on the raw SIM images of different illumination orientations can realize the lateral isotropic spectrum expansion (detailed in Section S5), of which the high-frequency components can be continuously increased and eventually converged after several iterations (Figs. S2d - S2f). Since the above operations are performed under a unified framework, the transmission of errors is avoided, which helps to obtain the optimal solution.

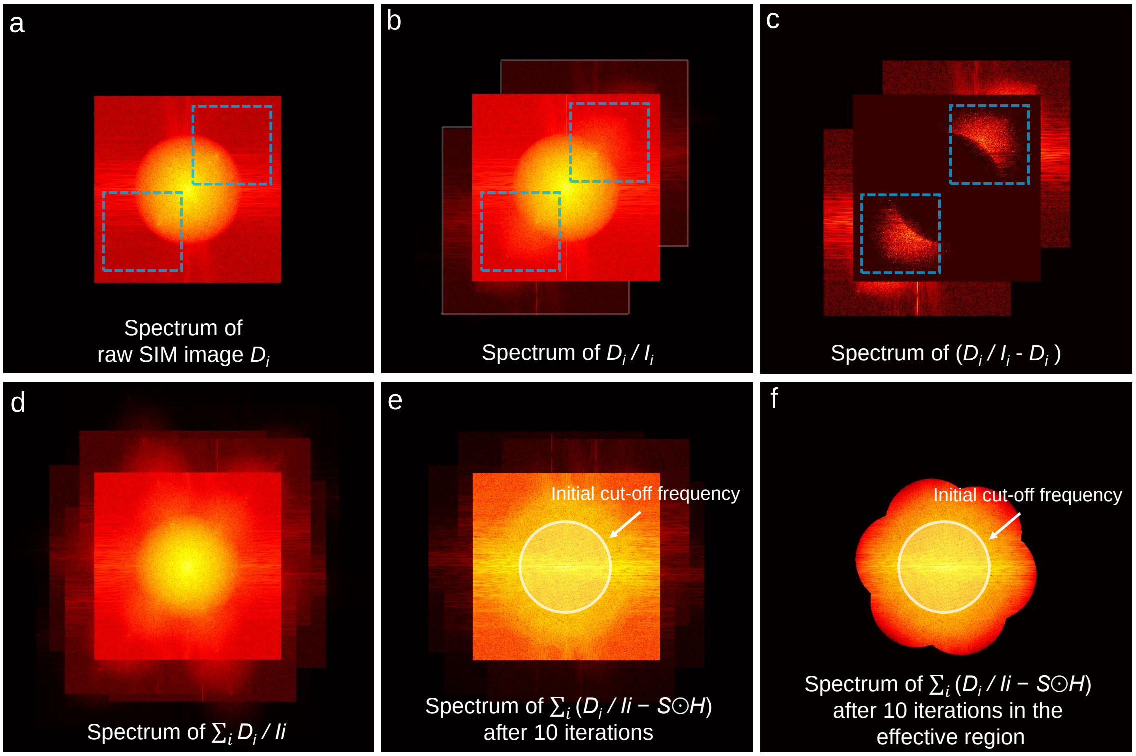

Figure S2. **Schematic diagram of the principle of spectrum expansion achieved by FP-SIM. a** The spectrum map of the raw SIM image D_i of a specific illumination orientation. Raw data are from Fig. 3 in the main text. **b** The spectrum map of D_i/I_i. As seen in the blue dashed box, the ±1-order spectrum components are shifted and the spectrum support domain is expanded. **c** The spectrum map of $D_i/I_i - D_i$, from which the enhancement of the high-frequency component can be seen more obviously. **d** The spectrum map of $\sum\limits_i D_i/I_i$. By jointly performing the operation of D_i/I_i on the raw SIM images of different illumination orientations, isotropic spectrum extension in the lateral direction can be achieved. **e** The spectrum map of $\sum\limits_i [D_i/I_i - H \odot S^k]$ after 10 iterations. **f** The spectrum map of $\sum\limits_i [D_i/I_i - H \odot S^k]$ after 10 iterations in the theoretically effective support domain. After several iterations, the high-frequency components will be continuously increased and eventually converged

S5. Convergence discussion of Fourier ptychographic structured illumination microscopy

Next, we will analyze whether Eq. S17 contributes to the minimization of the optimization function (Eq. 1 in the main text). The main cost function of Eq. 1 in the main text can be defined as follows:

$$\varepsilon = \sum_i \left\| \mathscr{A}[\hat{S}(\mathbf{r})] - D_i(\mathbf{r}) \right\|_p^2 \tag{S18}$$

where $\|\|_p$ indicates the l_p vector norm, $\hat{S}$ is the approximate solution, and $\mathscr{A}[\hat{S}(\mathbf{r})]$ can be further represented as $[I(\mathbf{r}) \cdot \hat{S}(\mathbf{r})] \odot H(\mathbf{r})$. For l_p-norm fidelity terms in fluorescence SIM, the dominant noise source is photon shot noise, which follows a Poisson distribution. While a Poisson-likelihood fidelity is physically accurate[5,6], the l_2 squared fidelity term is generally preferred over l_1 because it better approximates the Poisson statistics for typical photon counts and enables stable, efficient optimization. In contrast, l_1 is more suitable for sparse or outlier-type noise, which is not dominant in fluorescence SIM[7]. Consequently, many reconstruction algorithms adopt l_2 to achieve robust reconstruction with computational simplicity[2,8,9]. In the case of l_2 norm, if the modulation of PSF is not considered, the gradient of ε with respect to S can be expressed as:

$$\frac{\partial \varepsilon}{\partial S(\mathbf{r})} = 2I_i(\mathbf{r}) \sum_i \{Dec[D_i(\mathbf{r})] - I_i(\mathbf{r})\hat{S}(\mathbf{r})\} \tag{S19}$$

To minimize the error of the loss function of Eq. S19, one can use fixed-point iteration by setting the gradient to zero ($\partial \varepsilon / \partial S(\mathbf{r}) = 0$). For the simplest gradient descent method, the object function can be updated based on the following equation, taking into account the expansion of the system detection passband, by incorporating the illumination inversion step (D_i/I_i):

$$S^{k+1}(\mathbf{r}) = S^k(\mathbf{r}) + 2\alpha \sum_i \{Dec[D_i(\mathbf{r})]/I_i(\mathbf{r}) - S^k(\mathbf{r})\} \tag{S20}$$

where α represents the step-size. If α is set to 0.5 and the deconvolution process for $\mathscr{A}(\hat{S})$ and D_i in Eq. S19 is operated in a joint manner, Eq. S17 can be approximately equivalent to Eq. S20:

$$2\alpha \sum_i \{Dec[D_i(\mathbf{r})]/I_i(\mathbf{r}) - S^k(\mathbf{r})\} + S^k(\mathbf{r}) \approx Dec \sum_i [D_i(\mathbf{r})/I_i(\mathbf{r}) - H(\mathbf{r}) \odot S^k(\mathbf{r})] + S^k(\mathbf{r}) \tag{S21}$$

It should be noted that the step size $\alpha = 0.5$ provides a good balance between convergence stability and speed: it avoids the oscillation or divergence that may occur with $\alpha = 1$, while maintaining faster convergence compared to smaller step sizes. Since there is at least 39.1% overlap between neighboring sub-apertures, which is more than the aperture overlapping percentage in conventional FPM[10], the resulting data redundancy can provide guarantee for iterative convergence (Fig. S3). It should be noted that although the above convex optimization theory based on gradient descent cannot fully analyze the non-convex super-resolution reconstruction problem, such a solution has proven to be effective for practical applications in conventional FPM[11]. In addition, we used a series of preprocessing and regularization processes to further ensure the convergence of FP-SIM, which are detailed in Sections S7-S9.

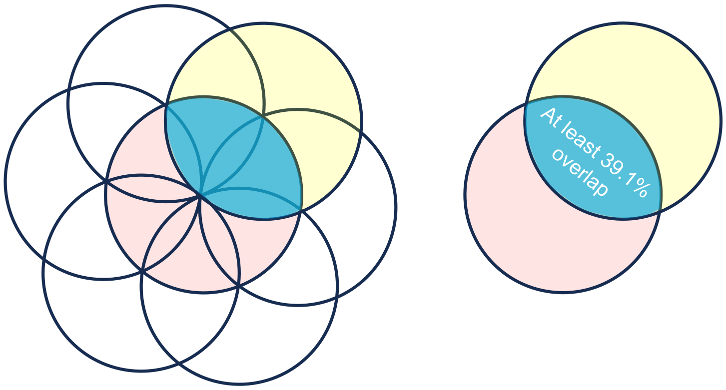

Figure S3. Overlap of different Fourier-domain sub-apertures in SIM. Considering the most extreme case, *i.e.*, when the illumination frequency is matched to the system cutoff frequency, the overlap ratio of adjacent sub-apertures is approximately 39.1%. In other cases, *i.e.*, when the illumination frequency is less than the system cutoff frequency, the overlap is greater than 39.1%.

S6. Analysis on the uniqueness of the solution of Fourier ptychographic structured illumination microscopy

The uniqueness of the solution for iterative reconstruction using only three SIM images has been demonstrated, but the premise is that the illumination pattern is known[12]. In our method, the illumination pattern I has been acquired in advance, and under such conditions, if the system PSF is not considered, the only unknown is the sample information S for a raw SIM image in a certain illumination orientation. Since SIM images in different illumination orientations jointly contain the same unknown term, the use of a total of three images is sufficient to ensure the uniqueness of the super-resolution solution. It should be noted that despite the deviations between the extracted illumination pattern and the actual one, based on the above discussions on super-resolution performance and convergence (Sections S4 and S5), a stable convergence to a high-quality super-resolution solution can be achieved through iterations with the addition of a series of preprocessing and regularization, as shown in Fig. 2 of the main text. See Sections S7-S9 for more details on preprocessing and regularization.

Regarding the noise immunity, for the conventional 9-frame SIM reconstruction, the extended high-frequency component in a certain illumination orientation is acquired by the three three-step phase-shifting SIM images in that orientation. When performing spectrum merging, the diffraction-limited wide-field information is jointly contributed by nine images in all illumination orientations, meaning that this component has a higher signal-to-noise ratio (SNR), while the high-frequency components are still contributed by only three images in their respective orientations. Although there are non-uniform overlaps between the high-frequency components of different illumination orientations, these overlaps rarely assist in improving the SNR, but instead cause problems for subsequent image reconstruction, resulting in a non-uniform synthetic spectrum. In FP-SIM, all high-frequency components are co-contributed by three SIM images, so it is actually comparable to the conventional 9-frame reconstruction method in terms of SNR. In addition, since FP-SIM jointly solves the high-frequency information of the three illumination orientations in a unified iterative framework, it facilitates a better overall performance compared with the conventional scheme of solving them individually first and then merging them.

S7. Preprocessing based on Richardson-Lucy deconvolution

Richardson-Lucy (RL) deconvolution[13] is an iterative filtering algorithm specifically for Poisson noise, which is derived from Bayesian theory according to the maximum likelihood (ML) principle. In statistical probability, the conditional probability of estimating a clear image from a blurred version can be expressed as:

$$p(f|g) = \frac{p(g|f)p(f)}{p(g)} \tag{S22}$$

where $p(g)$ represents the blurred image captured by a linear imaging system, $p(f)$ denotes the ideal image, and $p(g|f)$ is the PSF that causes blurring. Considering that the image pixels are independent of each other, according to the Poisson statistical model, Eq. S22 can be rewritten as:

$$p(g|f) = \prod_{(x,y)} \frac{h(x,y) \odot f(x,y)^{g(x,y)} e^{-h(x,y) \odot f(x,y)}}{g(x,y)!} \tag{S23}$$

where $f(x,y)$ represents the ideal image, $h(x,y)$ denotes PSF, and $g(x,y)$ is the blurred image. In order to obtain the maximum conditional probability, according to ML, first take the logarithm of Eq. S23:

$$\ln p(g|f) = \sum_{(x,y)} \{g(x,y) \ln[h(x,y) \odot f(x,y)] - \ln[h(x,y) \odot f(x,y)] - \ln[g(x,y)!]\} \tag{S24}$$

Then, take the derivative of $f(x,y)$ in Eq. S24 and set the result to 0:

$$f(x,y) = \left[\frac{g(x,y)}{h(x,y) \odot f(x,y)} \odot h(x,y)'\right] f(x,y) \tag{S25}$$

where $h(x,y)' = h(-x,-y)$. By introducing the concept of iterative update in Eq. S25, the general form of RL deconvolution is obtained:

$$f^{n+1}(x,y) = \left[\frac{g(x,y)}{h(x,y) \odot f^n(x,y)} \odot h(x,y)'\right] f^n(x,y) \tag{S26}$$

where f^{n+1} and f^n denote the estimated values of the ideal image in the $n+1$-th and n-th iterations, respectively, and f^{n+1} will asymptotically converge to the ideal image according to the probability. In this work, we use RL deconvolution to pre-process each original SIM image to remove some Poisson noises as well as partial out-of-focus backgrounds, and set the default number of iterations to 5 for combined efficiency and performance considerations[14].

It is worth mentioning that RL deconvolution can enhance the peaks of the first-order spectrum of the raw illumination image when testing the sample with strong periodicity or under the TIRF-SIM mode[13], which assists the illumination pattern extraction in FP-SIM (note that the spectrum peak can also be obtained by means of calibration in advance, which is detailed in Section S12).

S8. Centre-notched Hanning filter to obtain the initial estimate

In conventional iterative SIM algorithms, usually the wide-field image obtained by averaging the multi-step phase-shifting image superposition is used as the initial estimate of the iteration, but this still introduces image redundancy[15]. In order to obtain a well-defined initial estimate of the super-resolution image while minimizing the original acquisition frames, we use a centre-notched Hanning window function to extract a high-contrast initial image directly from a single frame illumination image. The proposed centre-notched Hanning filter is as follows (note that the orientation subscript is omitted here for simplicity):

$$Hann_{Norch} = \frac{|DTF(Hann)|^{T} \cdot |DTF(Hann)|}{\max^{2}|DTF(Hann)|}\{1 - \frac{W_{Str}}{1.05} exp[-(\frac{\mathbf{k}}{0.5W_{Width}})^{2}]\} \tag{S27}$$

$$Hann = \frac{1}{2}[1 - \cos(|\mathbf{k}_{ex}|\pi r_{x})] \tag{S28}$$

where $Hann_{Norch}$ represents the used centre-notched Hanning filter, DTF denotes the discrete Fourier transform operation, $Hann$ is a regular Hanning window with the strongest attenuation at the 1-order spectrum of the illumination image, superscript T is the transpose operation, W_{Str} and W_{Width} denote the strength and width of the central attenuation in the notch filter, r_x is the spatial coordinate along the x-axis, and $r_x \in [-|\mathbf{k}_{ex}|, |\mathbf{k}_{ex}|]$. Here $\mathbf{k}_{ex}$ can be replaced by the original cut-off frequency of the system, because the illumination frequency is usually close to the cut-off frequency to maximize the super-resolution effect. For the parameters of the notch filter, W_{Width} was fixed at 1, while W_{Str} varied from 0 to 1 to control the attenuation strength, with $W_{\mathrm{Str}} = 1$ indicating the maximum notch effect[14]. In fact, the main energy of the illumination modulation in the spectrum map of the original SIM image is concentrated at the peak of the 1-order spectrums. Therefore, a Hanning window with a passband capable of filtering the first-order spectrums can be adopted to attenuate the illumination modulation while suppressing the ringing effect caused by spectrum leakage. However, the Hanning window also attenuates the relatively high-frequency information of the sample and amplifies the low-frequency signal. For this issue, a centre-notched filter is compounded with the Hanning window to suppress some out-of-focus backgrounds, which indirectly compensates for the high-frequency information of the sample. Figure S4 illustrates the original SIM image and the initial estimations obtained by different filtering operations, where Fig. S4a is the original full-field SIM image, and Fig. S4b is the magnified image from the boxed region in Fig. S4a, Fig. S4c is the wide-field image acquired by averaging the multi-step phase-shifting original SIM images, Fig. S4d is the original SIM image after RL deconvolution, and Fig. S4e and S4f are the initial estimates of the iteration obtained from the regular Hanning window and the centre-notched Hanning window, respectively. Compared to the wide-field image acquired by multi-step phase-shifting original SIM images, the initial estimate obtained by the centre-notched Hanning window has better contrast and does not need to capture additional phase-shifting images.

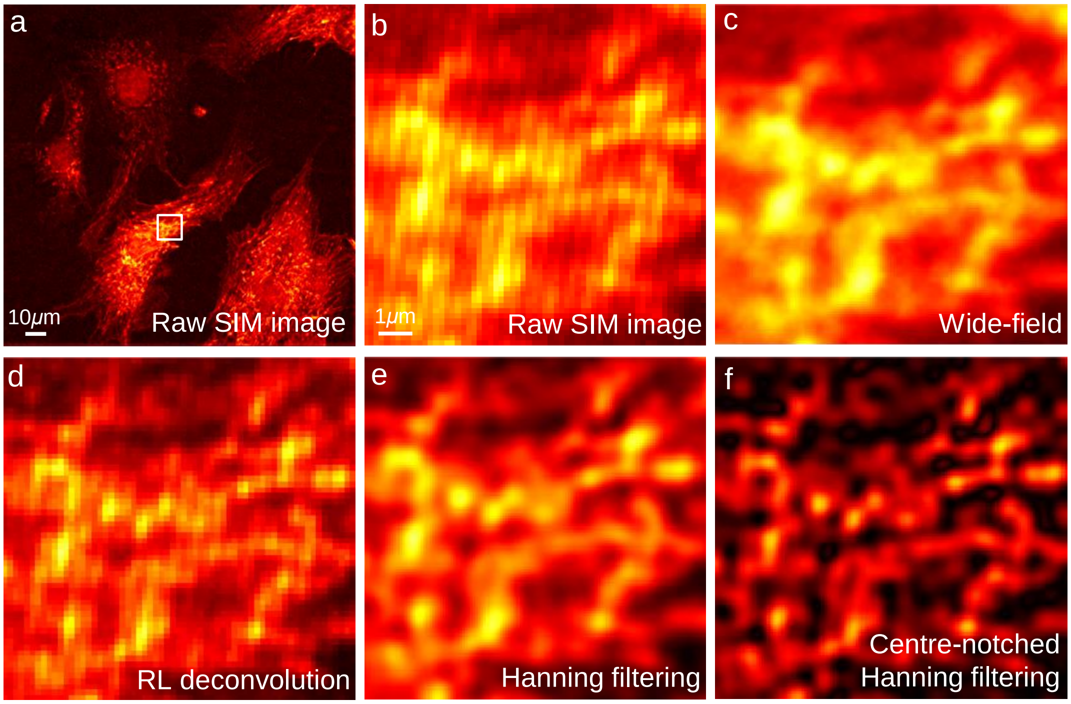

Figure S4. Original SIM image and initial estimation obtained by different filtering operations. a The original full-field SIM image. The image is from the simulation data in Fig. 2 of the main text. **b** The magnified image from the boxed region in **a**. **c** The wide-field image acquired by averaging the multi-step phase-shifting original SIM images. **d** The original SIM image after RL deconvolution. **e** The initial estimate of the iteration obtained from the regular Hanning window. **f** The initial estimate of the iteration obtained from the centre-notched Hanning window. Scale bars: 10 μm (**a**); 1 μm (**b-f**)

S9. Regularization on target spectrum support

During the iterations, we impose a regularization constraint on the objective function so that it can converge to the expectation faster and with fewer iterations, which is essential to normalize the originally ill-posed inverse problem. In SIM, the extension of the sample high-frequency information is directly related to the orientation and frequency of the illumination pattern, and the limit of the super-resolution spectrum is theoretically the sum of the original cutoff frequency and the illumination frequency. Based on this condition, the regularization term $R(S)$ is defined as:

$$R[S(\mathbf{r})] = S(\mathbf{r}) \odot \mathscr{F}^{-1}[Fre_{reg}(\mathbf{k})] \tag{S29}$$

$$Fre_{reg}(\mathbf{k}) = \begin{cases} 0 \quad if \quad \mathbf{k} > k_{cutoff} + \mathbf{k}_{ex} \\ 1 \quad else \end{cases} \tag{S30}$$

where k_{cutoff} represents the original cutoff frequency and Fre_{reg} denotes the mask that constrains the spectrum range. Note that $\mathbf{k}_{ex}$ in Eq. S30 is of integer-pixel accuracy. The regularization term effectively avoids the overflow of the wrong spectrum and the generation of high-frequency noise in the iteration process by limiting the spectrum range of the target function to a reasonable region, allowing it to rapidly approximate toward the desired one. Figure S5 illustrates the spectrum maps and super-resolution images before and after regularization. After 20 iterations without regularization, there is no effective increase in the high-frequency detail of the target object; instead, it suffers from severe scattering noise (Fig. S5a). After applying the regularization, the super-resolved signal outside the cutoff frequency is enhanced as expected, and finally the objective function converges to a high-quality super-resolution result (Fig. S5b).

Note that the iteration of FP-SIM will be carried until a fixed point is reached, *i.e.* $S^{k+1} = S^k$, which can be monitored by the error map $\left\|S^{k+1} - S^k\right\|_p^2$ (where $\|\|_p^2$ indicates the l_p vector norm). In practice, the number of iterations is set directly by experience to 20. In addition, our regularization strategy does not include an explicit parameter to balance the data fidelity term and the prior term, as the constraint is intrinsically embedded in the reconstruction process itself.

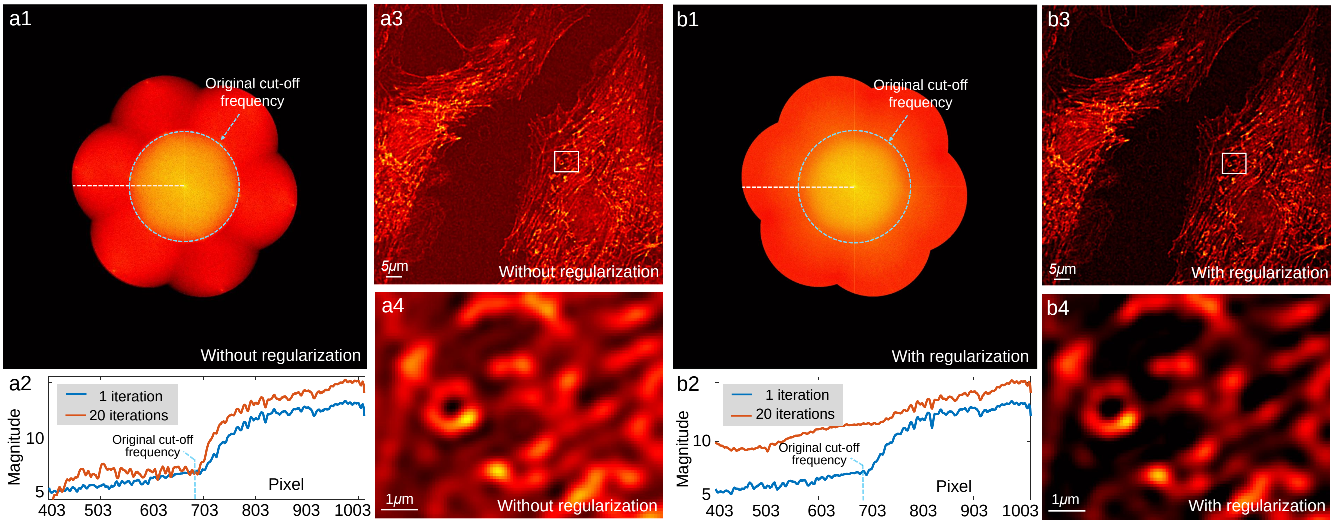

Figure S5. Spectrum maps and the corresponding super-resolution images with and without the regularization. a The spectrum map and the corresponding super-resolution image without the regularization, where **a1** is the spectrum map after 20 iterations, **a2** is the spectrum distribution curves of 1 and 20 iterations from the white dashed line in **a1**, **a3** is the super-resolution image corresponding to **a1**, and **a4** is the magnified super-resolution image from the boxed region in **a3**. The data is from the simulation data in Fig. 2 of the main text. **b** The spectrum map and the corresponding super-resolution image with the regularization. Scale bars: 5 μm (**a3**, **b3**); 1 μm (**a4**, **b4**)

S10. Comparative analysis of FP-SIM under different reduced-frame acquisition schemes

Under regular illumination schemes, existing frame-reduced SIM reconstruction algorithms can generally be categorized into two types. The first type extends the conventional 9-frame regression-based SIM algorithm. By assuming that the zero-order spectral components, which represent wide-field information, can be shared across different illumination orientations, the number of raw images required for SIM reconstruction can be reduced from nine to seven[16,17]. Although the frame reduction is limited, this category of methods provides relatively stable reconstruction performance. The second type abandons the conventional nine-frame algorithmic paradigm. Representative methods in this category include iFP[15], jRL[12], Bayesian estimation[18], and FD[19], which can further reduce the number of frames to four or even three. However, all these approaches rely fundamentally on the accurate acquisition of illumination parameters. In practice, such parameters are either estimated using the original phase-shifted dataset—thus failing to achieve true frame reduction throughout the entire reconstruction pipeline—or assumed to be known a priori, which limits their applicability in real experiments. Table S1 summarizes the principles and implementation details of these frame-reduced methods. It is noteworthy that the core step of FD-SIM corresponds to the Fourier-domain realization of the illumination inversion in our FP-SIM approach. Since the illumination patterns cannot be accurately extracted in experiments, FD-SIM often fails to achieve high-quality reconstruction through a one-step solution. In contrast, our proposed FP-SIM introduces iterative updates combined with a series of preprocessing and regularization strategies, enabling stable convergence toward a high-quality super-resolved solution. For details on the experimental comparison between these frame-reduction methods and FP-SIM, see Section S11.

In regular illumination schemes, the minimal number of frames required by FP-SIM is three, *i.e.*, one raw image per illumination direction without phase shifting. To investigate the influence of reduced-frame strategies, we gradually increased the frame number from 3 to 9 and evaluated reconstruction performance under different acquisition schemes. As illustrated in Fig. S6, six cases were compared: (1) three directions with three phase-shifted images each; (2) three directions with two phase-shifted images each; (3) two directions with two phase-shifted images each and one direction with a single image; (4) one direction with three phase-shifted images and the other two with only one image; (5) 3-frame FP-SIM plus an additional widefield image; and (6) 3-frame FP-SIM (one image per direction). Figures S6a and S6b present the reconstructed super-resolution images of simulated BPAE cells under these six conditions. The reconstructed images exhibit only minor differences, which are not readily discernible at the visual level. To quantitatively assess reconstruction fidelity, we calculated the structural similarity index (SSIM) and peak signal-to-noise ratio (PSNR) with respect to the ground-truth image, as well as the rolling Fourier ring correlation (rFRC) resolution[20] (Figs. S6c and S6d). The results indicate that although reconstruction quality improves with increasing frame numbers, the improvement is marginal. Specifically, when the frame number increased from 3 to 9, the median SSIM improved by only 0.024, the median PSNR by 1.01 dB, and the mean rFRC-estimated resolution by 2.22 nm. These results suggest that while additional frames can enhance reconstruction, the benefit is limited. In contrast, reducing the acquisition burden by a factor of three offers a more favorable balance between photon efficiency and imaging practicality.

Table S1. Implementation schemes of different frame-reduction SIM reconstruction methods

Frame-reduction method	Iterations	Frames	Illumination parameter estimation	Image reconstruction	Remarks
7-SIM[16]	Non-iterative	7	Derived from multiple phase-shifted images via correlation methods	A regression-based reconstruction similar to conventional 9-frame SIM	Stable but limited frame reduction
7-LSSIM[17]	Non-iterative	7	Derived from multiple phase-shifted images via correlation methods	A regression-based reconstruction similar to conventional 9-frame SIM	Stable but limited frame reduction
FD-SIM[19]	Non-iterative	4	Derived from multiple phase-shifted images via correlation methods	A reconstruction algorithm based on ordinary least squares technique	Limited practical performance
iFP-SIM[15]	200-500 iterations	4	Assumed to be known (initial phase unknown)	A modified incoherent Fourier ptychographic procedure	Valid only for brightfield imaging
jRL-SIM[12]	100-300 iterations	3	Assumed to be known	A joint Richardson-Lucy deconvolution algorithm	Sensitive to low SNR
Bayesian estimation for SIM[18]	Not specified	4	Derived from multiple phase-shifted images via correlation methods	A Bayesian inverse-problem formulation approach	Sensitive to modulation parameters

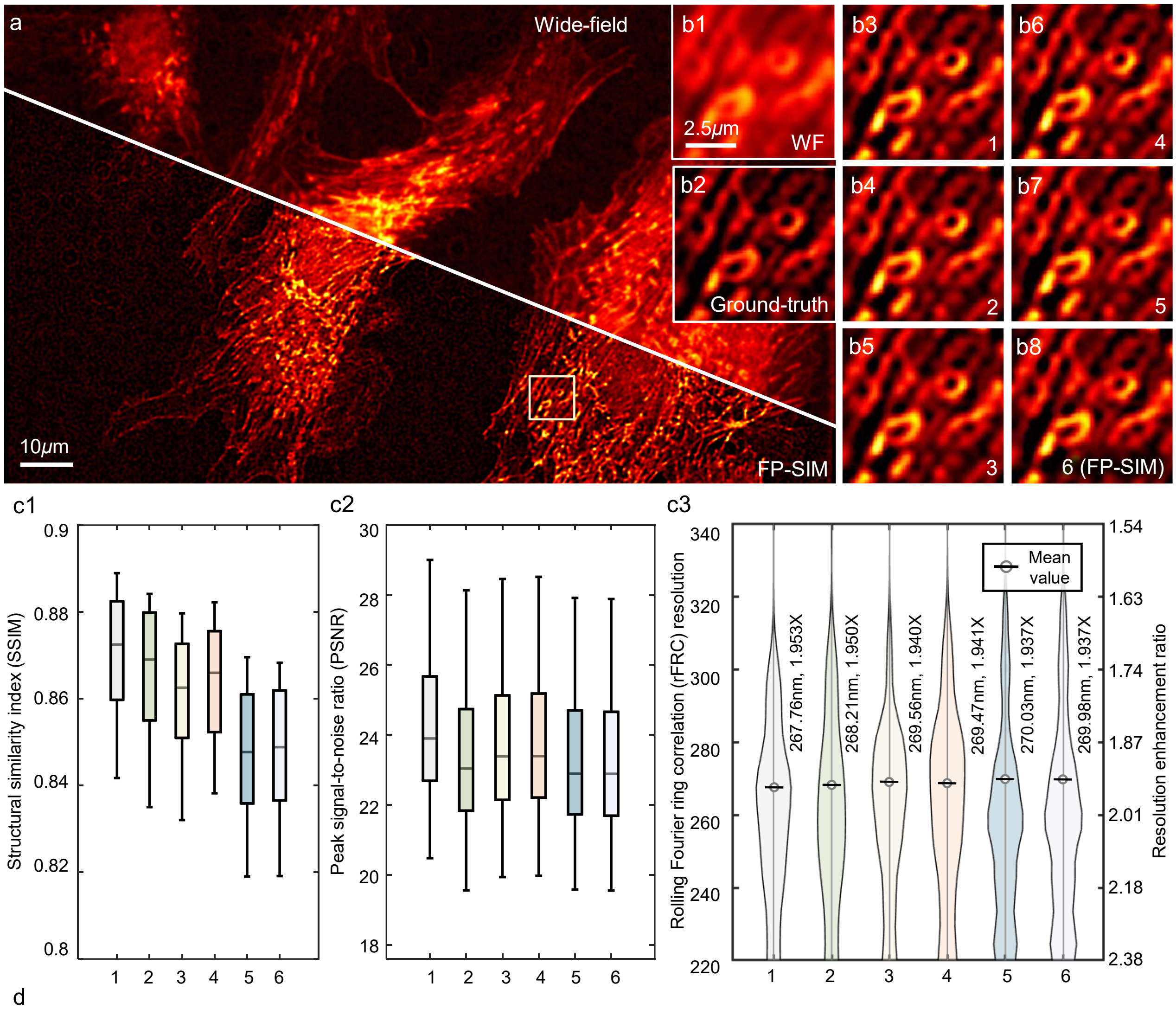

d

Index	Acquired raw images	Resolution enhancement ratio (Ratio of rFRC mean resolution between widefield image and super-resolution image)	SSIM (Median)	PSNR (Median)
1	3 directions x 3 phases	1.953	0.8725	23.899
2	3 directions x 2 phases	1.950	0.8695	23.042
3	2 directions x 2 phases + 1 direction x 1 phase	1.940	0.8625	23.387
4	1 direction x 3 phases + 2 direction x 1 phase	1.941	0.8659	23.395
5	3 directions x 1 phase + WF	1.937	0.8476	22.894
6	3 directions x 1 phase	1.937	0.8488	22.890

Figure S6. FP-SIM reconstruction results under different reduced-frame acquisition strategies. a Wide-field image of simulated BPAE cells and the corresponding super-resolution image reconstructed using 3-frame FP-SIM. **b** Magnified views of the yellow-boxed region in **a**, showing the wide-field image and super-resolution reconstructions obtained with different frame numbers. **c** Quantitative evaluation of FP-SIM reconstructions under different frame numbers in terms of SSIM, PSNR (with respect to the ground truth), and rFRC resolution. **d** Median SSIM and PSNR values, together with the mean rFRC resolution, corresponding to the results in **c**. Scale bars: 10 μm (**a**); 2.5 μm (**b**)

S11. Supplementary simulations and experiments

Supplementary simulations

Here we provide more simulation results to further verify the effectiveness of FP-SIM. Figure S7a-S7e illustrates the spectrum maps and the corresponding super-resolution images after different times of iterations for 10 dBW Gaussian noise power of the simulation experiments (Fig. 2) in the main text. As the iteration times increase, the high-frequency information of the sample exceeding the original cutoff frequency is gradually enhanced and converges as the iteration times close to 20, while the details of the super-resolution image are continuously refined, which also indirectly weakens the initial estimation artifacts caused by the slight ringing effect (regions marked by yellow triangles, where the structure sizes are smaller than the theoretical improved lateral resolution). Note that in order to compare the spectrum variations for different times of iterations, the display threshold of the spectrum maps here is different from the rest of the text. Although visually, the low-frequency component is significantly higher than the recovered high-frequency one, the spectrum profile in Fig. S7e1 indicates that the high-frequency information is significantly enhanced compared with the original, and the final converged spectrum profile is already close to the distribution of the ideal super-resolution OTF. Regarding why the high-frequency component looks weaker than the low-frequency, we think that since FP-SIM performs the gradual recovery and enhancement of super-resolution information on the basis of the original wide-field image, the low-frequency wide-field component still retains its original distribution, with higher energy density than the high-frequency information recovered under certain constraints.

We also used the modified incoherent Fourier ptychographic method[15] (iFP, a method for reducing image acquisition) for the same simulation data. As shown in Fig. S7f, due to the lack of precise extraction of the actual illumination parameters, which is particularly severe in the case of extremely dense gratings, each iteration does not contribute to an effective resolution improvement despite the iterative compensation of the illumination pattern, but instead leads to reconstruction artifacts. In addition, since iFP obtains the initial estimate of uniform illumination by averaging multi-step phase-shifting images, it is inferior in quality and efficiency (image redundancy) compared to our approach, in which the initial estimate is obtained by RL deconvolution and a centre-notched Hanning filter from a single-frame raw SIM image.

To more intuitively demonstrate the advantages of FP-SIM, we performed super-resolution image reconstruction of structured illumination images of simple ring structures using FP-SIM, iFP, the conventional 9-frame reconstruction algorithm (COR-based parameter estimation and Wiener deconvolution-based image reconstruction, here we directly call it conventional 9-SIM method for the sake of simplicity), and the high-fidelity SIM technique by point-spread-function engineering[14] (Hifi-SIM, a state-of-the-art SIM reconstruction algorithm), respectively (Fig. S8). Similar to the generation of the simulated data in Fig. 2 in the main text, an image of simple ring structures was used as the ground truth. We multiplied the sinusoidal fringe patterns (with the frequency matching the cutoff frequency of a 0.85 NA objective) with the ground truth. The modulated images were then convolved with a simulated OTF to simulate the original SIM images acquired with a 40× 0.85 NA objective. Finally, Gaussian noises of different powers were added to the simulated SIM images. In the noise-free case, the 9-frame reconstruction algorithms (conventional 9-SIM and Hifi-SIM) obtained high-quality super-resolution reconstructions

(Fig. S8c1-S8c3). For the iterative approaches, iFP failed to resolve the rings in detail (Fig. S8c4), while FP-SIM optimized super-resolution images of comparable quality to the 9-frame reconstruction algorithms through only 3 original illumination images (Fig. S8c5-S8c6). With the increase of the noise, the results obtained by the conventional 9-SIM suffered from severe reconstruction artifacts (Fig. S8d-S8g). Although Hifi-SIM alleviated these artifacts, the ring structure of the sample was still impaired. In contrast, FP-SIM yielded relatively higher-quality reconstruction images at low signal-to-noise ratios (SNRs), performing superior robustness to noise.

Supplementary experiments

Static experiments

First, quantification experiments on fluorescent microspheres are supplemented as shown in Fig. S10. The experimental results indicate that FP-SIM achieves a lateral resolution of about 99.35 nm with only three raw SIM images at 100×, 1.45 NA objective and 525 nm fluorescence, which is slightly inferior to the 96.89 nm of conventional 9-SIM.

Next, based on the experimental data shown in Fig. 3 (BPAE cells acquired with our custom-built system and microtubules from the publicly available BioSR dataset[21]) in the main text, we performed comparative studies under different frame-reduction strategies. Four representative approaches were considered for reconstruction, including iFP[15], jRL[12], FD[19], and FP-SIM. The reconstructed super-resolution images of BPAE mitochondria are presented in Figs. S11a and S11b. Results obtained by FD and FP-SIM are more consistent with those from conventional 9-frame SIM, whereas iFP and jRL exhibit pronounced artifacts. To quantitatively assess fidelity, we computed the structural similarity index (SSIM) and peak signal-to-noise ratio (PSNR) with respect to the 9-frame SIM reconstructions (Fig. S11c). FP-SIM achieved the best performance in both fidelity and noise-related metrics. In addition, rFRC resolution analysis (Fig. S11d) shows that FP-SIM provides a resolution enhancement comparable to conventional 9-frame SIM. The reconstruction results of microtubules are further illustrated in Figs. S11e–S11h, where FP-SIM also delivers superior overall performance relative to the alternative frame-reduction methods. Subsequently, another set of comparative experiments was performed on BPAE cells acquired with our custom-built SIM system (Fig. S12a). FP-SIM, iFP[15], conventional 9-SIM, and Hifi-SIM[14] were used to perform super-resolution reconstruction of the measured data, respectively. The inability to accurately estimate high-frequency illumination parameters and the effect of fluorescence noise on the actual imaging resulted in iFP failing to resolve mitochondrial details (Fig. S12b1-S12b2). Thanks to the accurate parameter estimation and professional image reconstruction steps as well as sufficient information sources, the 9-frame reconstruction methods (conventional 9-SIM and Hifi-SIM) distinguished these fine structures, but still with some noise-induced discontinuous granular artifacts whose size was below the theoretical enhanced lateral resolution, even though Hifi-SIM suppressed some artifacts and provided higher contrast (Fig. S12b3-S12b4). In contrast, FP-SIM extracted an initial estimate of the super-resolution image with higher contrast and sharper detail than the wide-field image only from a single original illuminated image through a series of preprocessing. With the simple and effective illumination parameter extraction, artifact-free, higher-quality super-resolution image was acquired from one-third of the data required for the 9-frame reconstruction methods with just a few (less than 15) iterations. In addition, we provided a set of reconstruction results using different methods (Hifi-SIM[14], FP-SIM and direct-SIM[22], which is an improved SIM reconstruction method without any prior knowledge of illumination patterns and bypassing the Wiener deconvolution procedures[22]) on microtubules of fixed COS-7 cells containing the severely defocused background (labeled by BODIPY^R FL goat anti-mouse IgG). Similarly, FP-SIM iteratively solved the parameter estimation and image reconstruction tasks in a joint framework from only three original observations, and acquired high-quality, artifact-free super-resolution images with better global performance (Fig. S13).

To test the generality of FP-SIM, we supplement the reconstruction results using FP-SIM on SIM images captured by N-SIM (a commercial microscope) under the TIRF mode. Figure S14 provides the super-resolution results obtained by different methods for the autofluorescent ascaris sample and labeled BPAE sample captured. For samples with mainly low-frequency information such as ascaris, FP-SIM still performed high-quality super-resolution reconstruction, with results comparable to those of N-SIM (Fig. S14a-S14c). For BPAE actin, which contained mainly high-frequency details, the N-SIM results suffered from some image artifacts, while FP-SIM avoided these artifacts and yielded better global performance by iteration (Fig. S14d-S14f).

We further evaluated the performance of FP-SIM under uneven illumination conditions using the endoplasmic reticulum (ER) images from the publicly available BioSR dataset[21]. Figures S15a1-S15a3 show the wide-field images obtained under each of the three illumination directions (averaged over the three phase-shifted images in each direction), illustrating pronounced intensity non-uniformity, particularly in the three regions of interest marked in the images. Averaging the images from all directions produces a balanced wide-field image (Fig. S15a4). The super-resolution image obtained by the 9-frame SIM (the ground truth provided in the BioSR dataset) also exhibit uniform intensity distribution (Fig. S15a5), as they integrate information from all three illumination directions. Similarly, FP-SIM leverages a reconstruction framework that iteratively incorporates images from all illumination directions, also resulting in a final super-resolution image with balanced intensity comparable to that of the 9-frame SIM (Fig. S15a6). Figures S15b-S15d present magnified views of the three regions of interest. For comparison, we reconstructed the super-resolution images using only a single illumination direction, with the corresponding results denoted as ‘Dn’ (n indicates the direction). When only one illumination direction is used for reconstruction, the resulting super-resolution images show pronounced intensity imbalance. In contrast, FP-SIM effectively mitigates this issue, yielding results with uniform intensity closely matching the ground truth. To further quantify the performance, we calculated SSIM between the reconstructed super-resolution images and the 9-frame SIM reference for the three regions of interest (Fig. S15e). These data demonstrate that FP-SIM effectively avoids the intensity imbalance caused by uneven illumination, achieving reconstruction uniformity comparable to 9-frame SIM.

An additional comparison was performed between FP-SIM and RL[13] as well as sparse deconvolution[23]. We used the BPAE mitochondria sample shown in Fig. 3 of the main text as the test specimen. Figures S16 a1-S16a4 present the wide-field image, the image after 20 iterations of RL deconvolution, the image after 100 iterations of sparse deconvolution, and the FP-SIM reconstruction, respectively. For clearer comparison, two regions of interest are enlarged in Figs. S16b and S16c. It can be seen that RL deconvolution yields only limited resolution improvement relative to wide-field imaging, whereas sparse deconvolution and FP-SIM achieve more significant enhancement. However, sparse deconvolution suffers from apparent detail loss in certain regions (highlighted by the arrows), despite its higher contrast. To further quantify the performance, we evaluated the rFRC resolution of these reconstructions and computed SSIM values relative to the conventional 9-frame SIM reference. The results demonstrate that both sparse deconvolution and FP-SIM markedly improve resolution, but FP-SIM provides substantially higher fidelity, producing results more consistent with the 9-frame SIM reference. It is worth noting that FP-SIM is not inherently incompatible with RL or sparse deconvolution. In practice, RL deconvolution may serve as a preprocessing step to suppress out-of-focus background prior to FP-SIM reconstruction, whereas sparse deconvolution can be incorporated as a postprocessing module to further refine the reconstructed results and enhance overall performance.

Live-cell dynamic experiments

We also supplement some live-cell experiments using FP-SIM. Figure S17 is a comparison of the wide-field images and the super-resolution images acquired by FP-SIM at certain time points in Supplementary Movie S1. As the imaging time increased, photobleaching became more severe and caused significant degradation of SNRs of the original SIM images. Note that the wide-field images shown in Fig. S17 were averaged from multiple phase-shifting images, which somewhat suppressed the noise. Therefore, the quality of the actual original SIM images was much worse. However, FP-SIM consistently maintained high-quality reconstruction performance, validating its superior noise immunity. In contrast, the results of Hifi-SIM show progressively more severe reconstruction artifacts (magnified images in the blue boxed regions). Figure S18 provides the super-resolution reconstruction results of live COS-7 mitochondria (labeled by MitoTracker^{TM} Green FM) at two specific time points obtained by PCA-SIM (structured illumination microscopy based on principal component analysis, a fast, non-iterative, high-quality, artifact-free, noise-robust SIM algorithm that allows real-time live-cell observation for complex experimental scenarios[24]) and FP-SIM . As can be seen from the results, FP-SIM achieves high-fidelity super-resolution reconstructions with a slight improvement in quality (regions pointed by blue arrows) over PCA-SIM for live cell data with low SNRs disturbed by severe out-of-focus background. These enhancements are due to the fact that the motion of the mitochondria itself between the three frames is lower than in the case of 9 frames, indicating that FP-SIM can somewhat avoid the effect of sample motion on the reconstruction results.

Time consumption of FP-SIM and real-time super-resolution imaging experiments

We ran the MATLAB code of FP-SIM through MATLAB R2016a using a Dell XPS 8930 computer (Intel(R) Core(TM) i7-9700 CPU, NVIDIA GeForce GTX 1660 Ti) and listed the time consumption of all super-resolution results in Tab. S2 (see Section S12 for the relevant open source code). The time consumption of FP-SIM is mainly related to the resolution of the original image. Since most of the iterative process of FP-SIM is performed pixel-by-pixel, it can be easily accelerated by GPU parallel processing. To demonstrate this potential, we implemented a preliminary accelerated version of FP-SIM based on C++, which can achieve real-time super-resolution imaging at about 3.75 frames per second at an original image resolution of 1024×1024, and 16.56 frames per second at a resolution of 512×512. Figure S19 shows the real-time imaging scene and results. The complete dynamic results are detailed in Supplementary Movie S2.

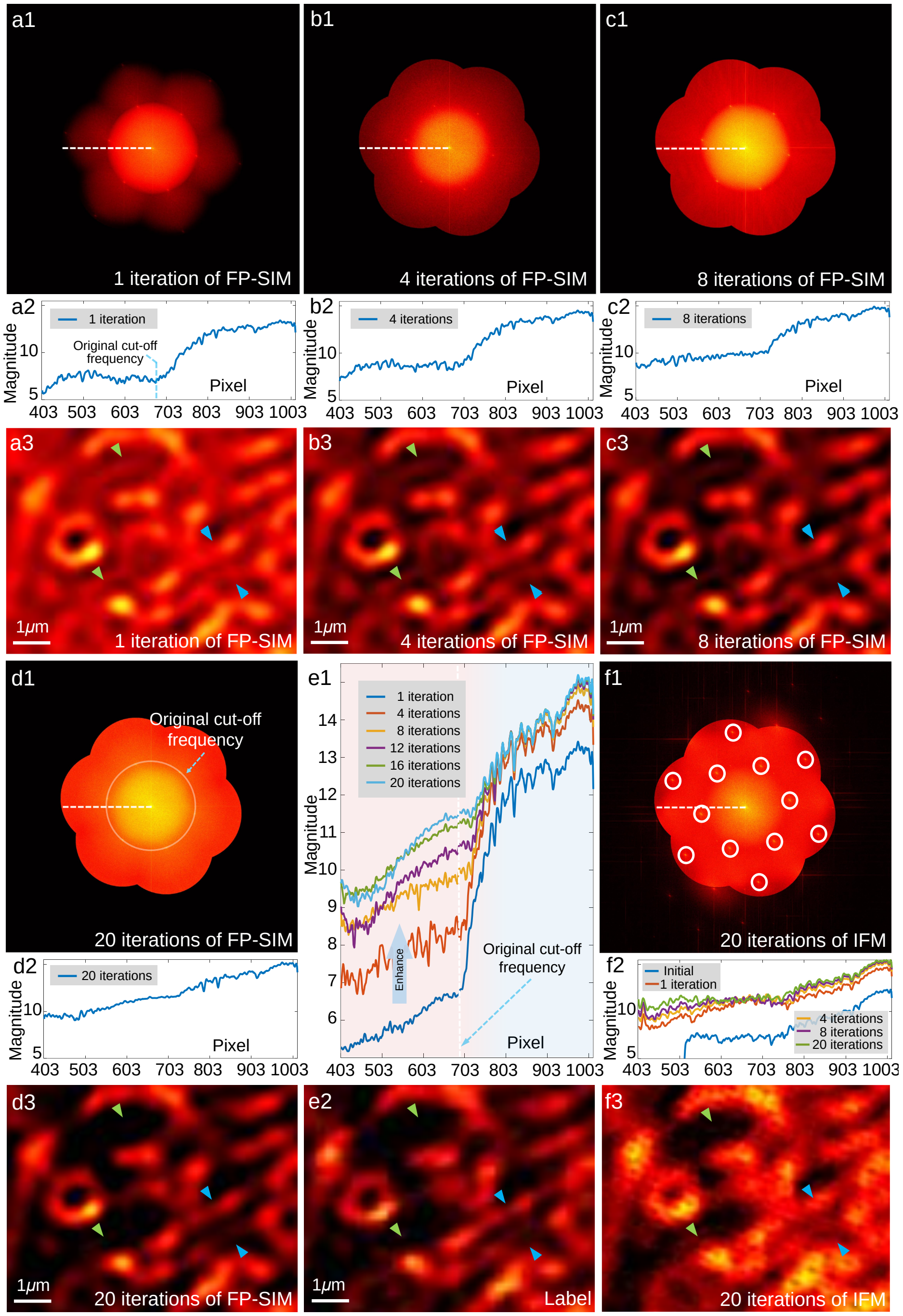

Figure S7. Spectrum maps and the corresponding super-resolution images of the simulated SIM data in the main text obtained by different iterative methods. a-e The spectrum maps and the corresponding super-resolution images after different times of FP-SIM iterations for 10 dBW Gaussian noise power of the simulation experiments in the main text, where **a1-d1** are the spectrum maps updated by different iterations of FP-SIM, **a2-d2** plot the spectrum distribution curves of the white dashed lines in **a1-d1**, and **a3-d3** are the magnified super-resolution images corresponding to **a1-d1** from the boxed regions in Fig. 2 of the main text. **e1** and **e2** are the spectrum distribution curves for different FP-SIM iterations and the ground truth, respectively. **f** The spectrum map and the corresponding super-resolution image obtained by IFP. Blue arrows point to regions where the artifacts caused by the ringing effect are gradually eliminated and green arrows point to regions where detail enhancement is more apparent. Experiments were repeated ten times independently with similar results. Scale bars: 1 μm (**a3-f3**)

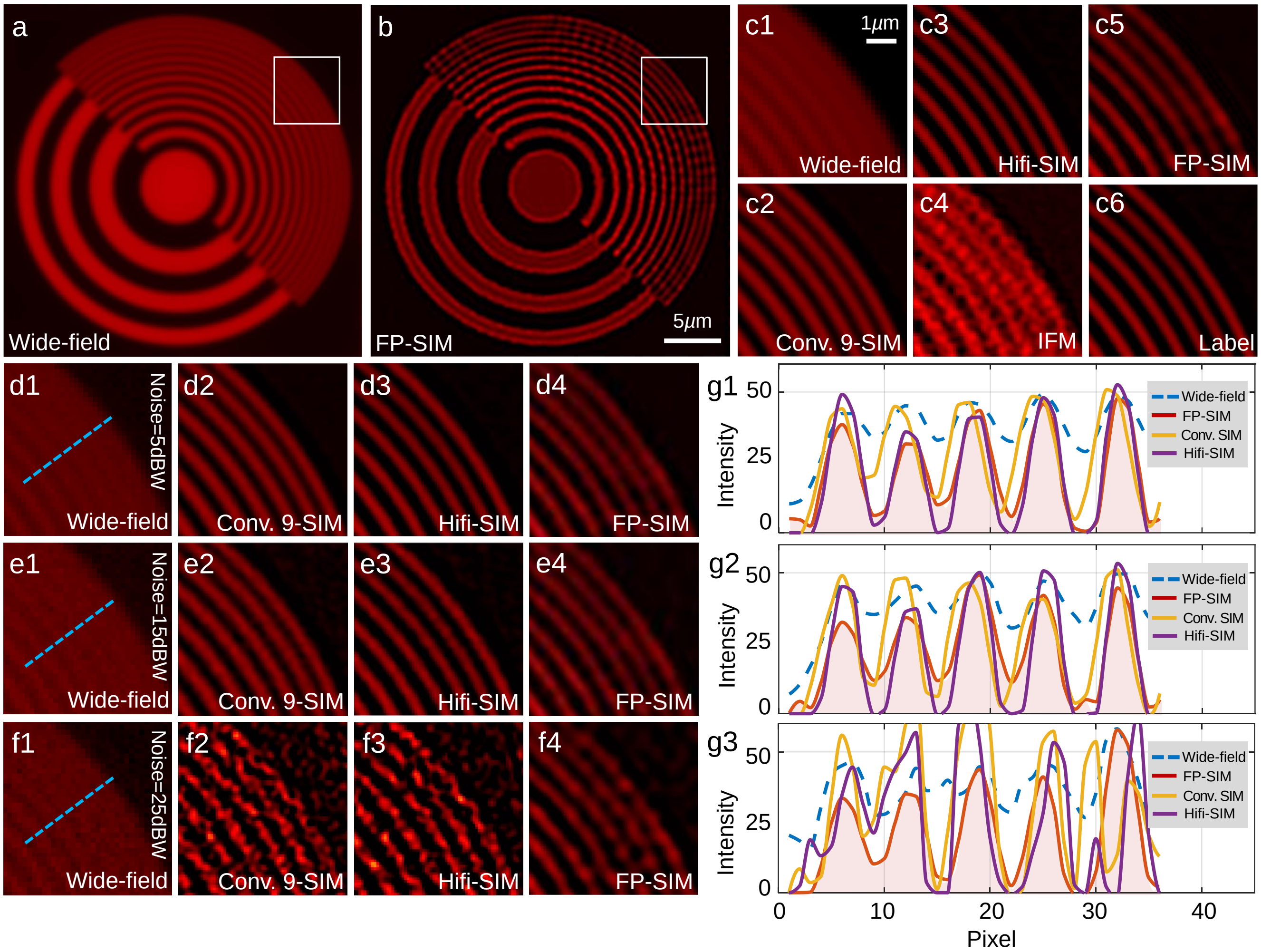

Figure S8. **Simulation results of different methods for SIM data of simple ring structures.** **a** Wide field image and the ground truth (bottom right). **b** Super-resolution image obtained by FP-SIM. **c** Magnified wide-field image (top left), super-resolution images from the boxed regions in **a** obtained by different methods (conventional 9-SIM, Hifi-SIM, IFP, and FP-SIM) and the ground-truth image. 'Conv.' represents 'Conventional'. **d** Magnified wide-field image (left) and super-resolution images from the boxed regions in **a** obtained by different methods (conventional 9-SIM, Hifi-SIM, and FP-SIM) when the noise is 5 dBW. **e** Magnified wide-field image (left) and super-resolution images from the boxed regions in **a** obtained by different methods (conventional 9-SIM, Hifi-SIM, and FP-SIM) when the noise is 15 dBW. **f** Magnified wide-field image (left) and super-resolution images from the boxed regions in **a** obtained by different methods (conventional 9-SIM, Hifi-SIM, and FP-SIM) when the noise is 25 dBW. **g** Intensity profiles along the light blue line in **d-f**. Experiments were repeated ten times independently with similar results. Scale bars: 5 μm (**a-b**); 1 μm (bottom right of **a**, **c-f**)

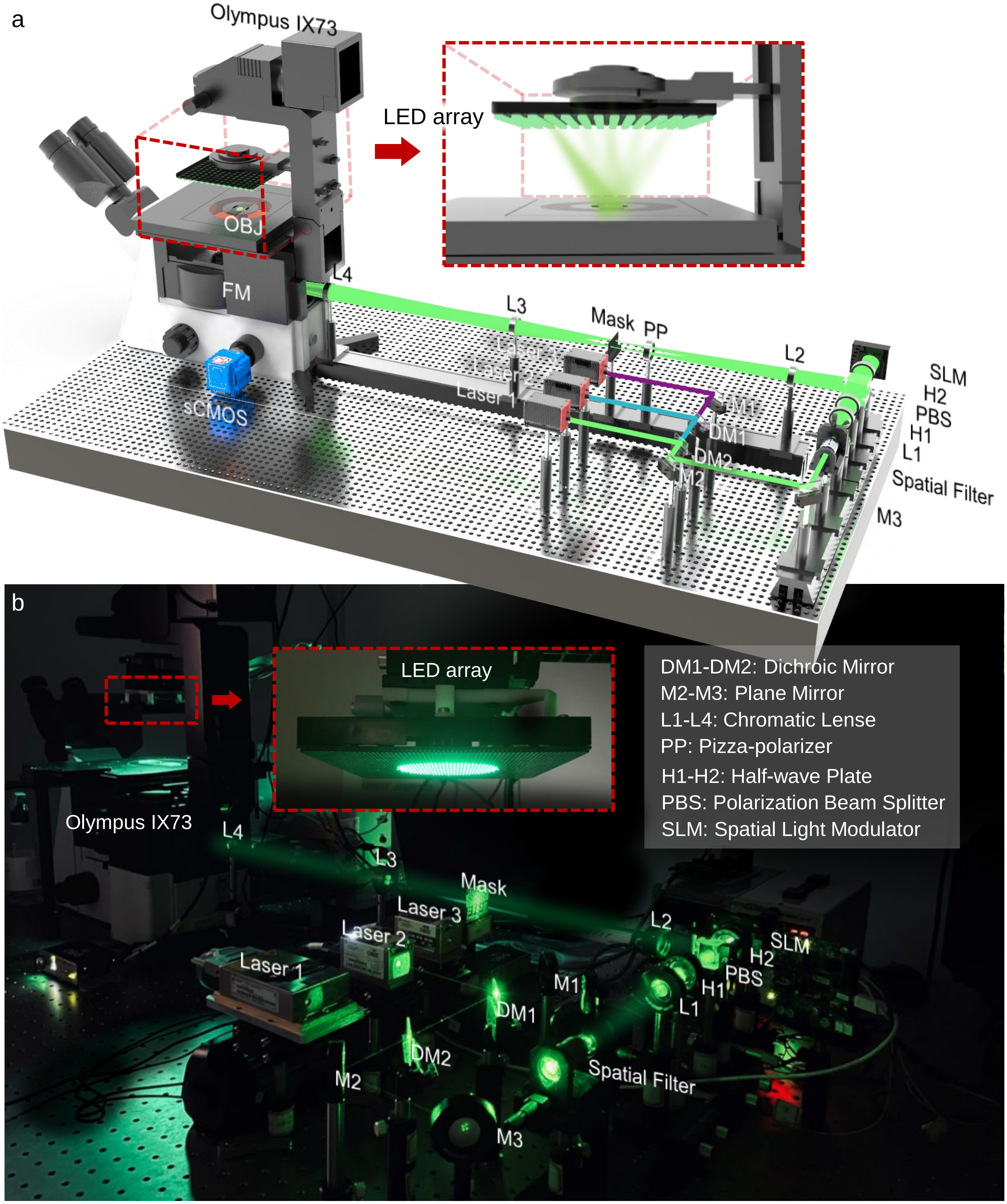

Figure S9. **The home-built tri-color SIM microscope**. **a** The schematic diagram of the tri-color SIM system. **b** The actual diagram of the tri-color SIM system.

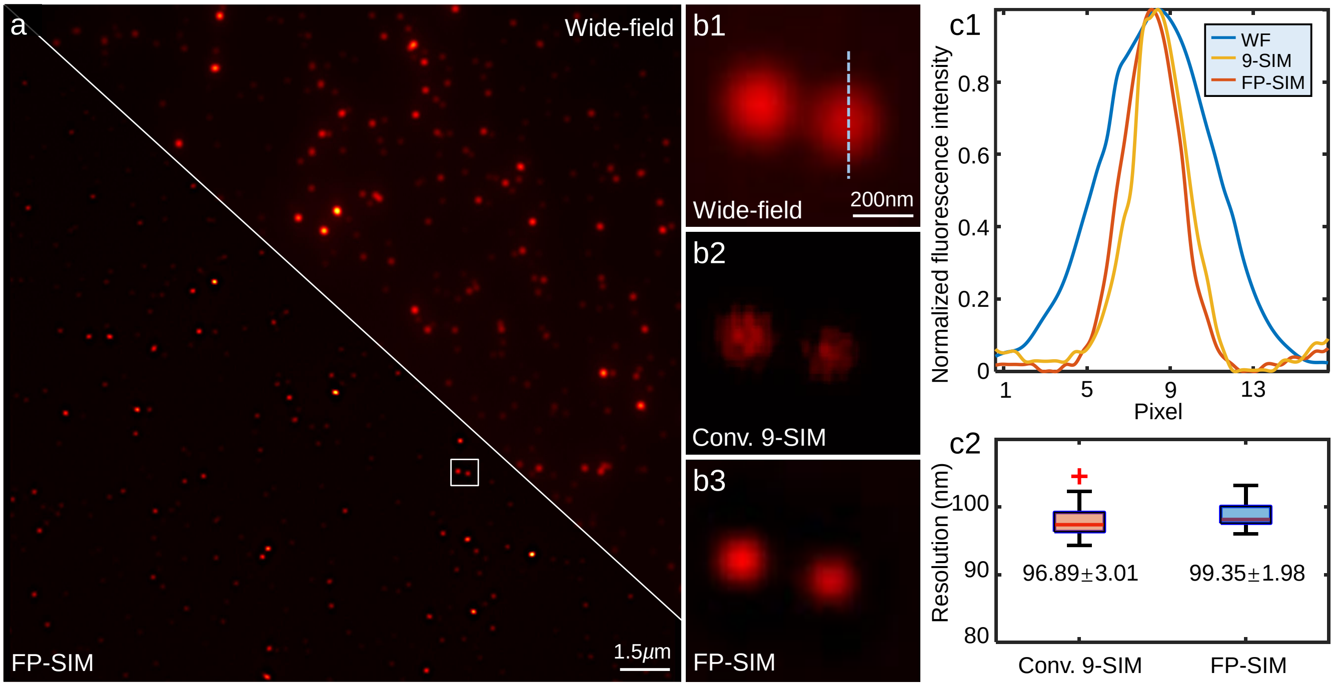

Figure S10. Comparative experiments on super-resolution results of fluorescent microspheres with 60 nm radius. **a** Comparison of the wide-field image and the super-resolution image obtained by FP-SIM. The wide-field image is displayed in the upper right triangle. The super-resolution image reconstructed by FP-SIM is shown on the lower left. The raw SIM images with a resolution of 345×345 were captured through a 100× objective (UPlanXApo 100×/1.45 Oil, Olympus, Japan). **b** Magnified wide-field image and super-resolution images of fluorescent microspheres from the boxed regions in (**a**) obtained by different methods (conventional 9-SIM and FP-SIM). **c** Intensity profiles along the light blue line in **b**. 'WF' represents 'Wide-field'. **d** Full width at half maximum of the fluorescence profiles of 10 microspheres in the reconstruction images of conventional 9-SIM and FP-SIM. Experiments were repeated ten times independently with similar results. Scale bars: 1.5 μm (**a**); 200 nm (**b**)

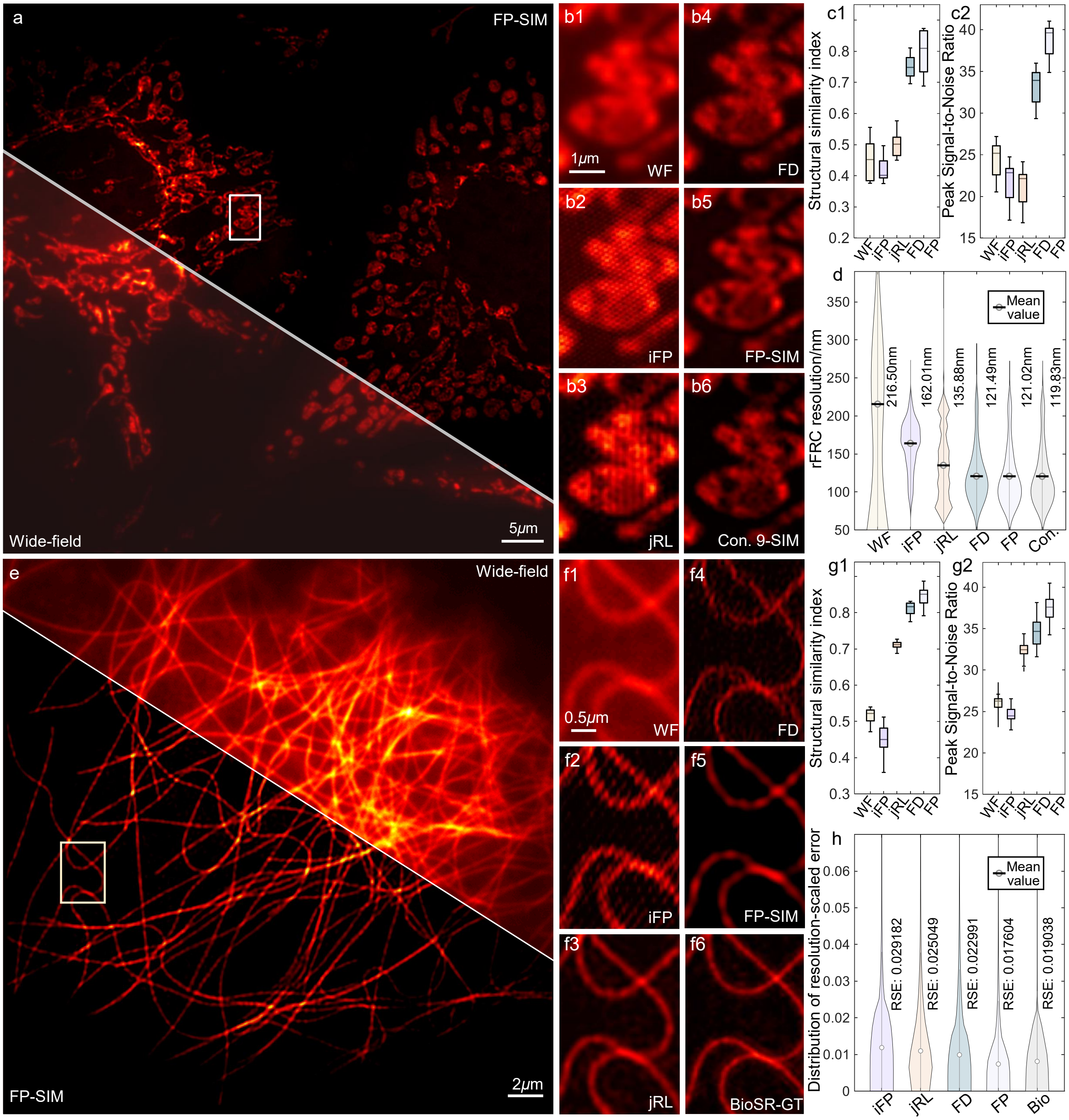
a
FP-SIM
Wide-field
5μm
b1
1μm
WF
b2
iFP
b3
jRL
b4
FD
b5
FP-SIM
b6
Con. 9-SIM
c1
Structural similarity index
0.2
0.3
0.4
0.5
0.6
0.7
0.8
WF
iFP
jRL
FD
FP
c2
Peak Signal-to-Noise Ratio
15
20
25
30
35
40
WF
iFP
jRL
FD
FP
d
Mean value
rFRC resolution/nm
50
100
150
200
250
300
350
216.50nm
162.01nm
135.88nm
121.49nm
121.02nm
119.83nm
WF
iFP
jRL
FD
FP
Con.
e
Wide-field
FP-SIM
2μm
f1
0.5μm
WF
f2
iFP
f3
jRL
f4
FD
f5
FP-SIM
f6
BioSR-GT
g1
Structural similarity index
0.3
0.4
0.5
0.6
0.7
0.8
WF
iFP
jRL
FD
FP
g2
Peak Signal-to-Noise Ratio
15
20
25
30
35
40
WF
iFP
jRL
FD
FP
h
Mean value
Distribution of resolution-scaled error
0
0.01
0.02
0.03
0.04
0.05
0.06
RSE: 0.029182
RSE: 0.025049
RSE: 0.022991
RSE: 0.017604
RSE: 0.019038
iFP
jRL
FD
FP
Bio

Figure S11. Comparative experiments on fixed BPAE mitochondria measured with our custom-built SIM system and microtubule samples from the BioSR dataset. a Wide-field image of BPAE mitochondria and the corresponding super-resolution image reconstructed by FP-SIM. The raw SIM images with a resolution of 1024×1024 were captured through a 100× objective (UPlanSApo 100×/1.40 Oil, Olympus, Japan). **b** Magnified view of the white-boxed region in **a** showing wide-field and super-resolution images reconstructed using different methods (iFP[15], jRL[12], FD[19], FP-SIM and conventional 9-SIM). **c** SSIM and PSNR between the super-resolution images in **a** and **b** and the reference 9-frame SIM reconstructions. **d** rFRC resolution distribution of the super-resolution images in **a** and **b** reconstructed using different methods. **e** Wide-field image of microtubules and the corresponding FP-SIM super-resolution image. The raw SIM images with a resolution of 502×502 were captured through a 1.3NA objective. **f** Magnified view of the yellow-boxed region in **e** showing wide-field and super-resolution images reconstructed using different methods. **g** SSIM and PSNR between the super-resolution images in **e** and **f** and the reference 9-frame SIM reconstructions. **h** RSE distribution of the super-resolution images in **e** and **f** reconstructed using different methods. Scale bars: 5 μm (**a**); 1 μm (**b**); 2 μm (**e**); 0.5 μm (**f**)

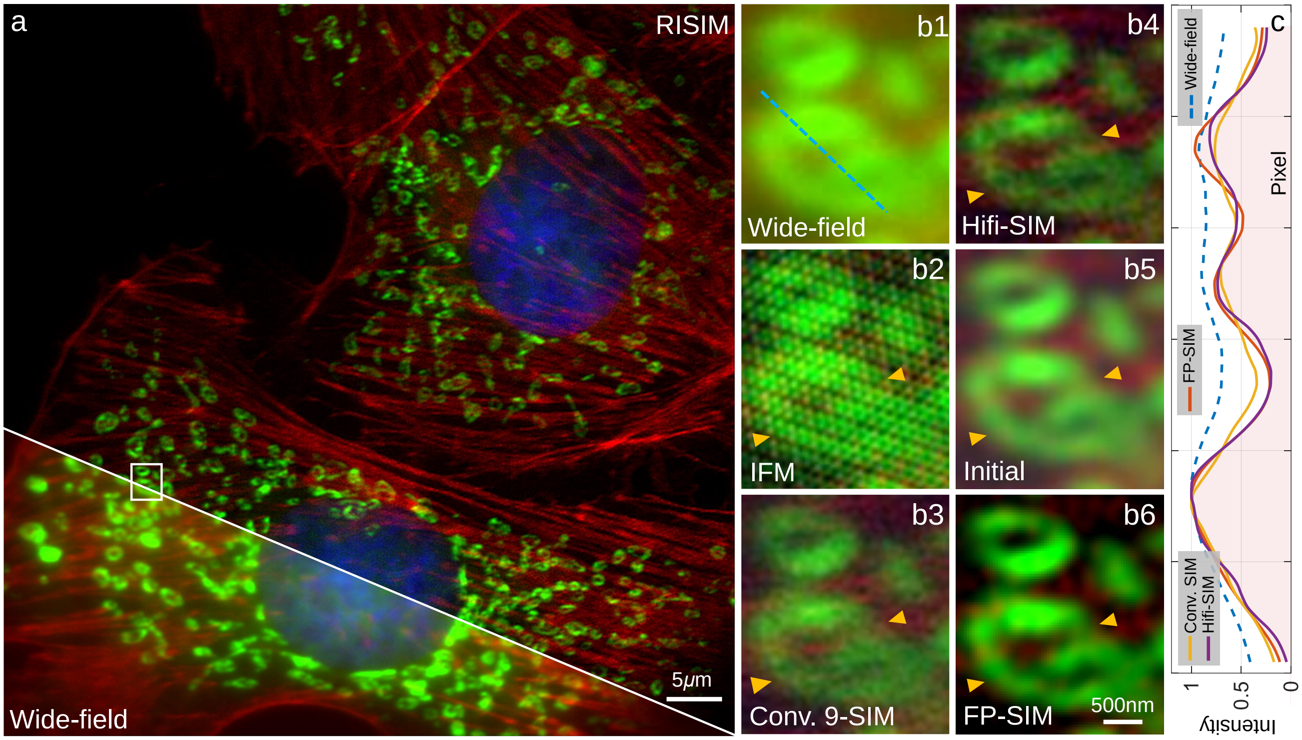

Figure S12. Comparative experiments on super-resolution results of a fixed BPAE cell sample with DAPI-labeled nucleus, Alexa Fluor^{TM} 568-labeled actin and MitoTracker^{TM} Green FM-labeled mitochondria. a Comparison of the wide-field image and the super-resolution image obtained by FP-SIM. The wide-field image is displayed in the upper right triangle. The super-resolution image reconstructed by FP-SIM is shown on the lower left. The raw SIM images with a resolution of 1024×1024 were captured through a 100× objective (UPlanSApo 100×/1.40 Oil, Olympus, Japan). **b** Magnified wide-field image (top left) and super-resolution images of mitochondria from the boxed regions in (**a**) obtained by different methods (IFP, conventional 9-SIM, Hifi-SIM, and FP-SIM (the initial estimation and the final iteration result)). **c** Intensity profiles along the light blue line in **b**. Yellow arrows point to regions where reconstruction differences are distinct. Experiments were repeated ten times independently with similar results. Scale bars: 5 μm (**a**); 500 nm (**b**)

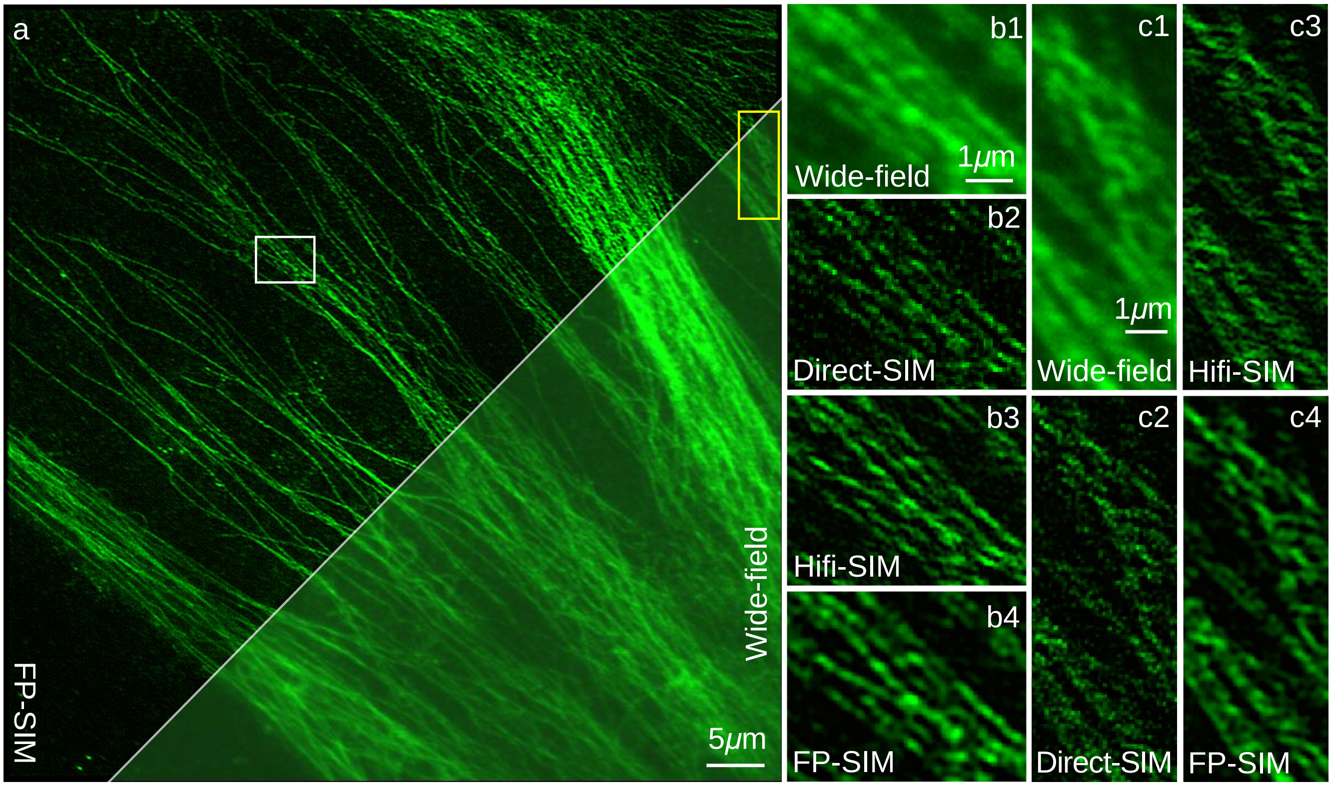

Figure S13. Comparative experiments on super-resolution results of microtubules of COS-7 cells labeled by BODIPY^R FL goat anti-mouse IgG. a Comparison of the wide-field image and the super-resolution image obtained by FP-SIM. The wide-field image is displayed in the lower right triangle. The super-resolution image reconstructed by FP-SIM is shown on the upper left. The raw SIM images with a resolution of 1024×1024 were captured through a 100× objective (UPlanXApo 100×/1.45 Oil, Olympus, Japan). **b** Magnified wide-field image and super-resolution images from the white boxed regions in (**a**) obtained by different methods (direct-SIM, Hifi-SIM and FP-SIM). C Magnified wide-field image and super-resolution images from the yellow boxed regions in (**a**) obtained by different methods. Experiments were repeated ten times independently with similar results. Scale bars: 5 μm (**a**); 1 μm (**b** and **c**)

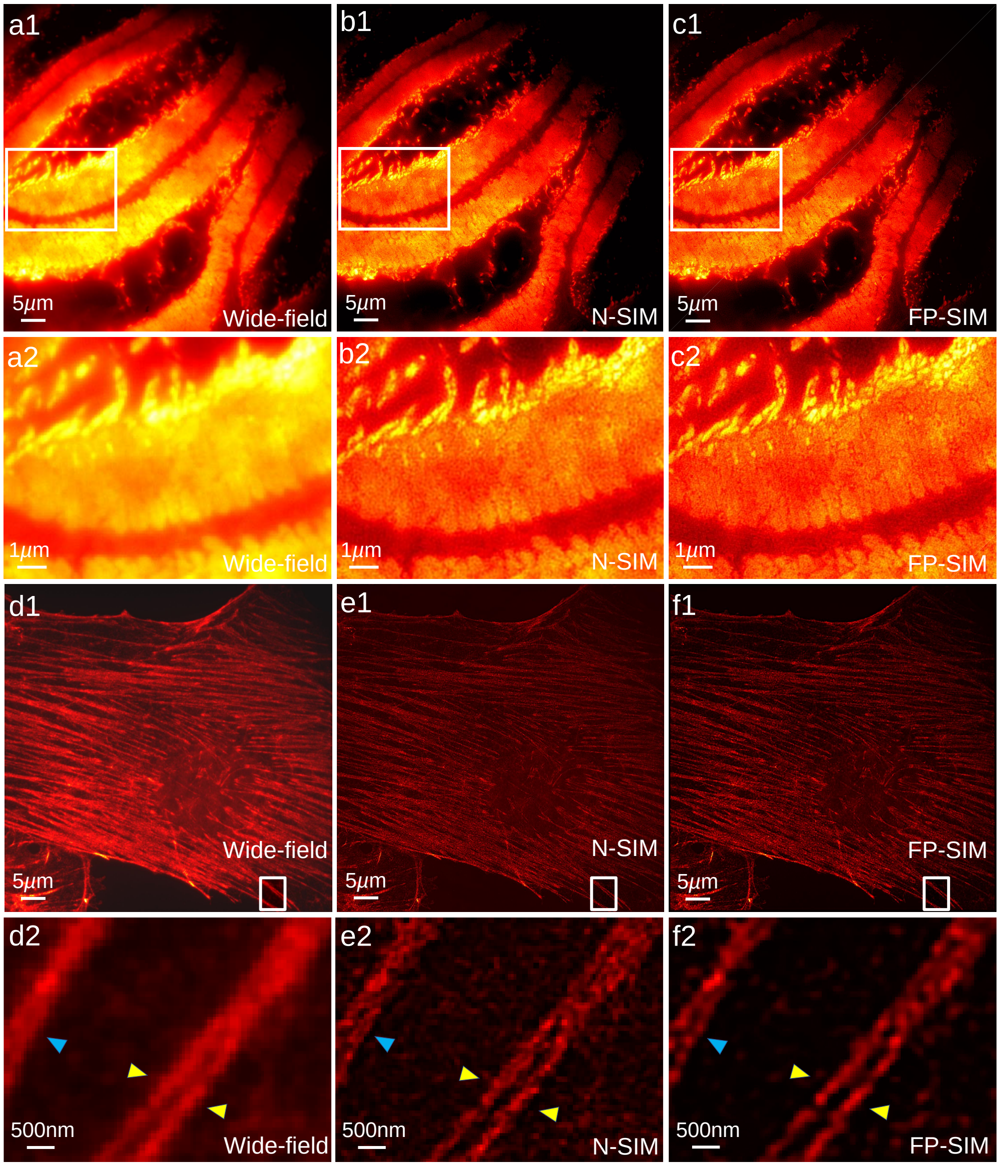

Figure S14. Comparative experiments on super-resolution results of the samples captured by N-SIM. a-c Wide-field image and super-resolution images of an autofluorescent ascaris obtained by different methods (N-SIM and FP-SIM), where **a2-c2** are the magnified images from the white boxed regions in **a1-c1**. **d-f** Wide-field image and super-resolution images of the BPAE actin obtained by different methods, where **d2-f2** are the magnified images from the white boxed regions in **d1-f1**. These raw SIM images with the resolution of 1024×1024 were captured through a 100× objective (CFI Apochromat TIRF 100× Oil, NA 1.49, Nikon, Japan) of N-SIM (Nikon, Japan). Note the data of the ascaris sample is from our previous work[24]. Yellow and blue arrows point to regions where reconstruction differences are distinct. Experiments were repeated ten times independently with similar results. Scale bars: 5 μm (**a1-c1**, **d1-f1**); 1 μm (**a2-c2**); 500 nm (**d2-f2**)

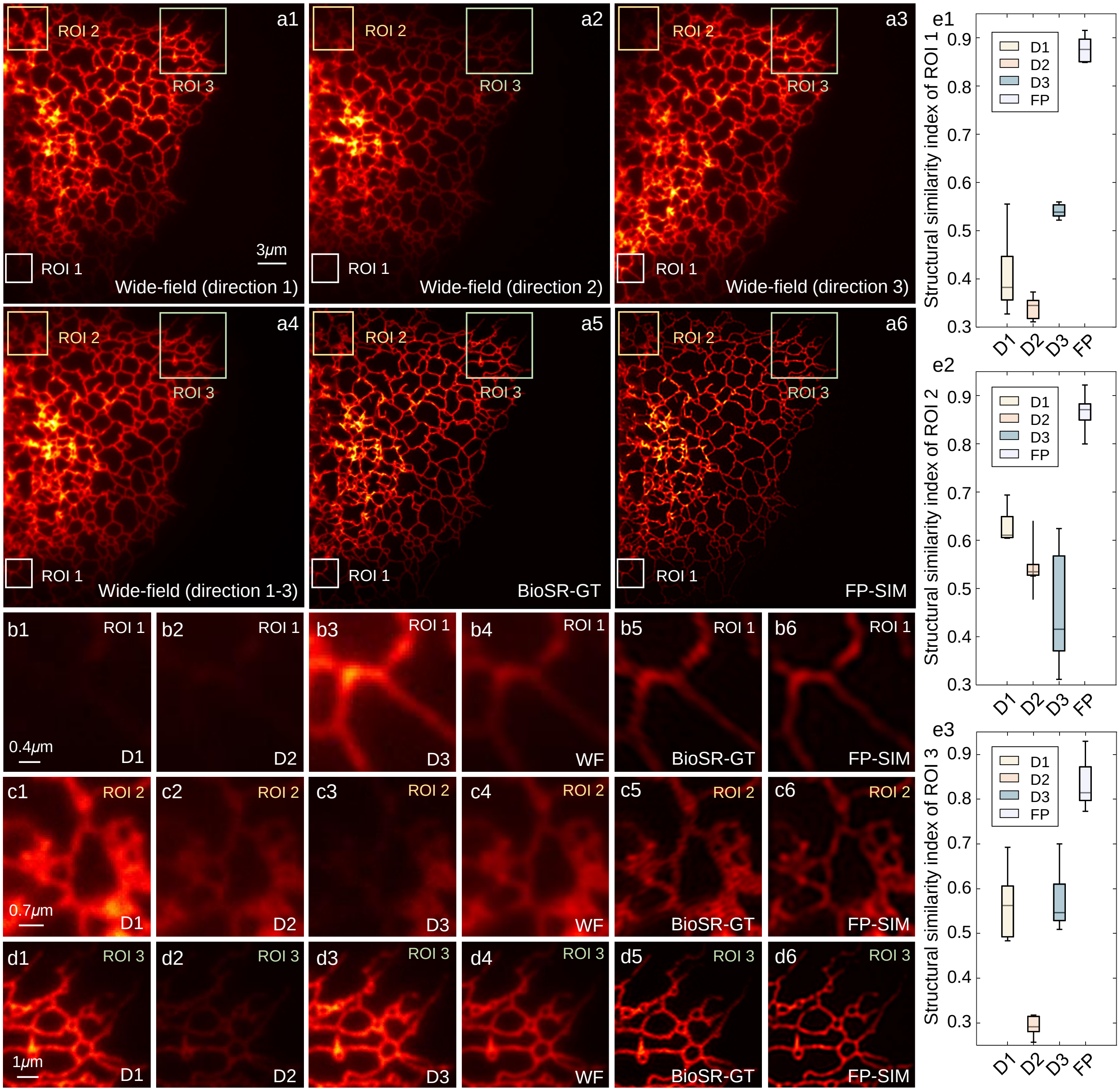

Figure S15. Experimental results of FP-SIM under uneven illumination from different directions. **a1-a3** Wide-field images obtained from single illumination directions (averaged over three phase-shifted frames). The raw SIM images with a resolution of 502×502 were captured through a 1.3NA objective. **a4** Wide-field image generated by averaging all illumination directions. **a5** Ground-truth super-resolution image from the BioSR dataset[21], obtained with 9-frame SIM. **a6** Super-resolution image reconstructed by FP-SIM. **b-d** Magnified regions of interest from **a**, comparing wide-field images and super-resolution reconstructions from different methods ('Dn' denotes reconstruction using only the nth illumination direction). **e** SSIM values between super-resolution reconstructions and the 9-frame SIM ground truth. Scale bars: 3 μm (**a**); 0.4 μm (**b-d**)

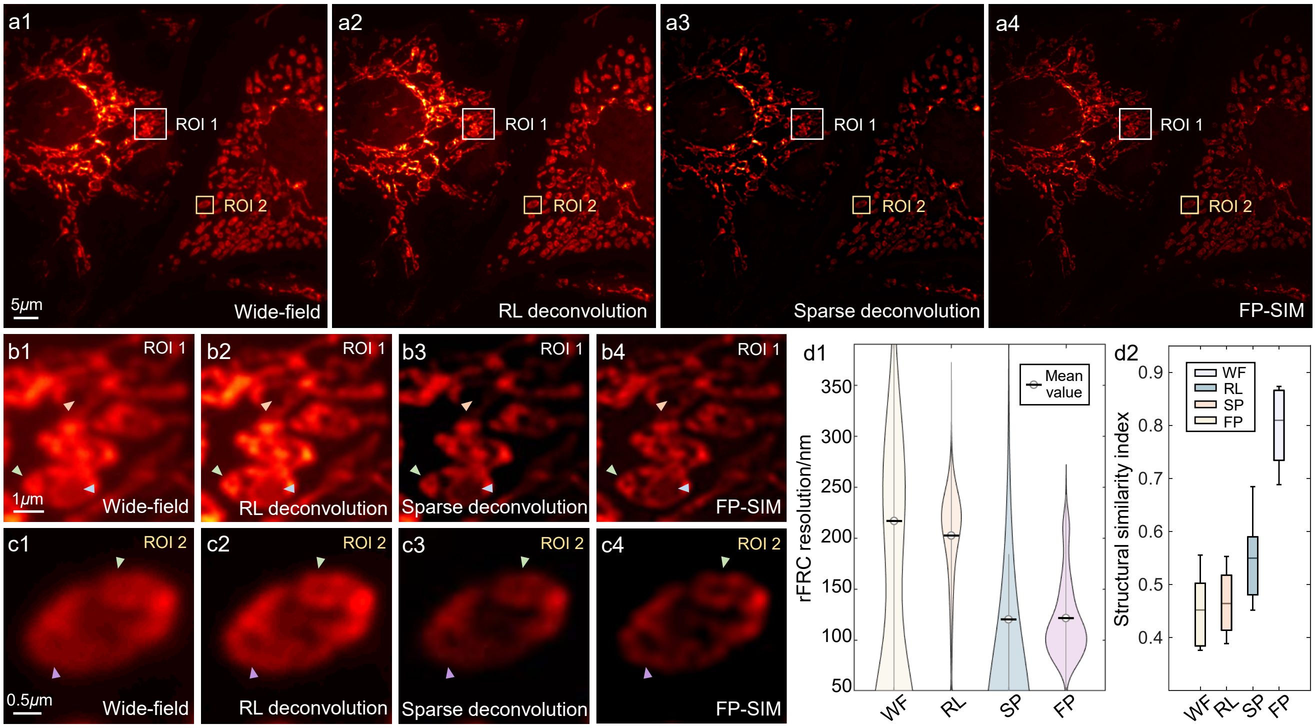

Figure S16. **Comparison of FP-SIM with RL and sparse deconvolution on BPAE mitochondria images acquired using the custom-built system. a1-a4** Wide-field image, result after 20 iterations of RL deconvolution, result after 100 iterations of sparse deconvolution, and super-resolution image reconstructed by FP-SIM. **b, c** Magnified views of the boxed regions in **a** obtained with different methods. **d** Distributions of rFRC resolution and SSIM values of the results from different methods relative to the conventional 9-frame SIM reference. Scale bars: 5 μm (**a**); 1 μm (**b**); 0.5 μm (**c**)

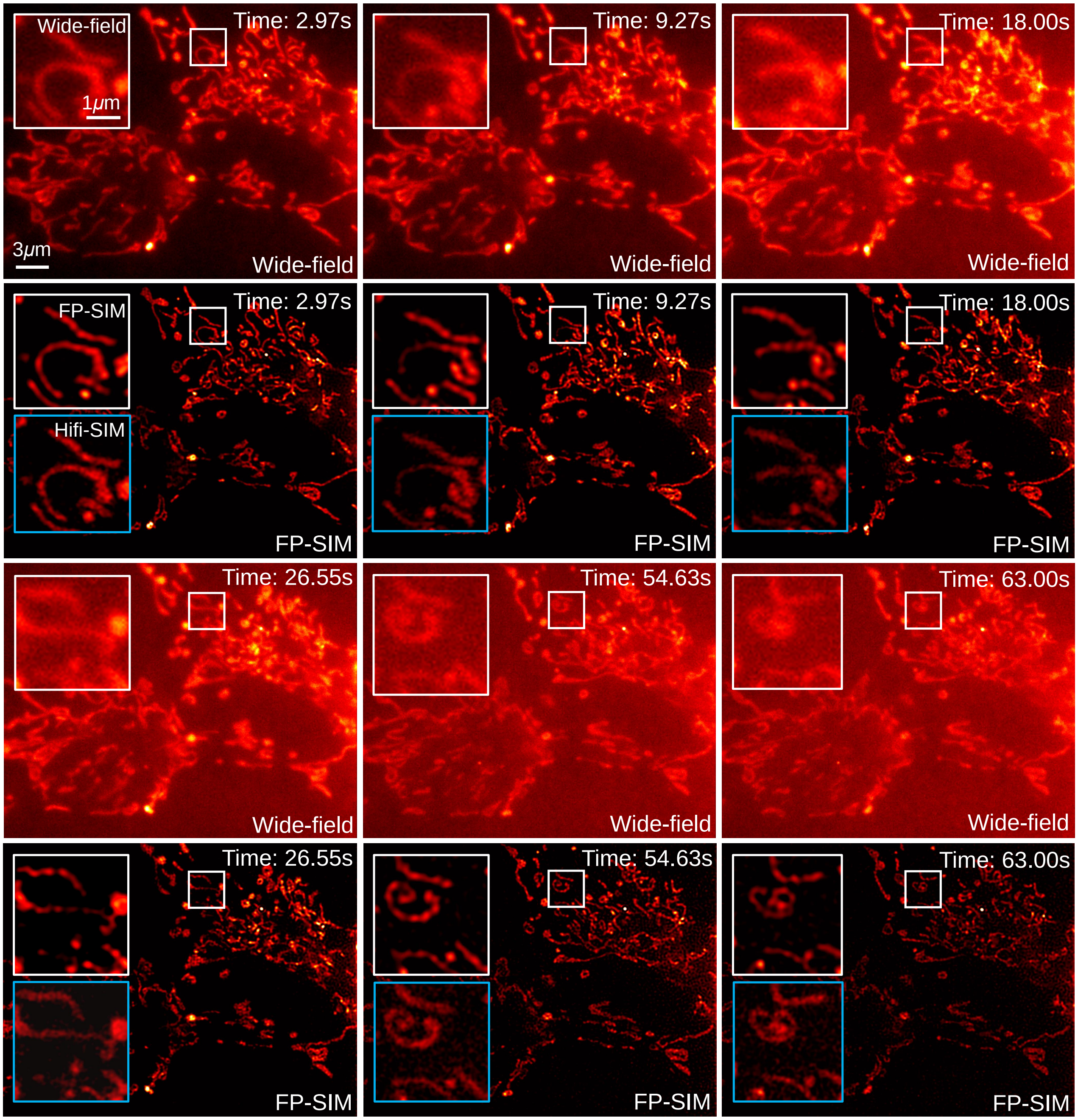

Figure S17. Super-resolution results of live COS-7 mitochondria labeled by PK Mito Red obtained by FP-SIM at different time points. As the imaging time increased, photobleaching became more severe and caused significant degradation of SNRs of the original SIM images, while FP-SIM consistently maintained high-quality reconstruction performance. In contrast, the results of Hifi-sim show progressively more severe reconstruction artifacts. Scale bars: 1 μm (magnified image); 3 μm (full-field image)

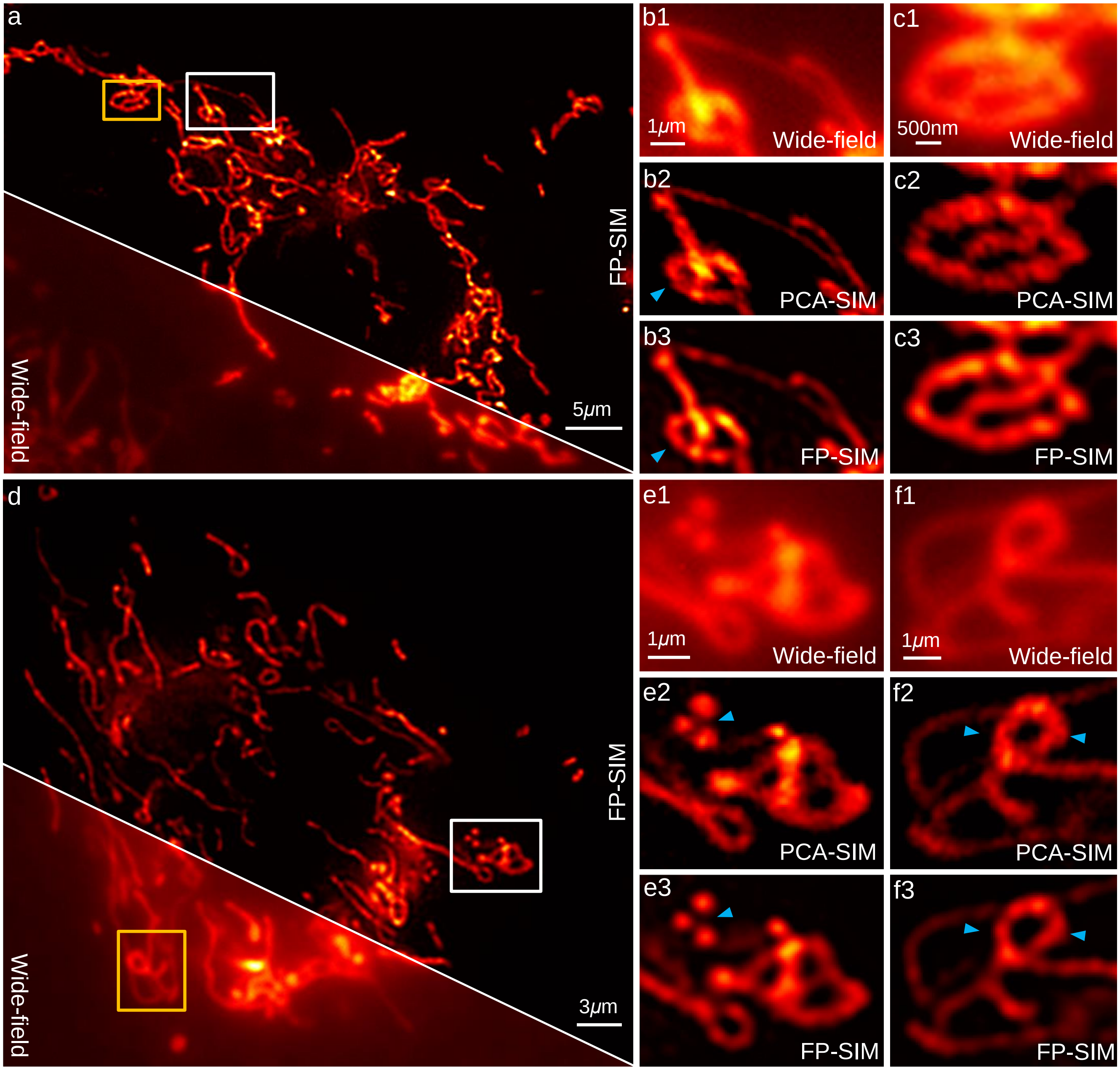

Figure S18. Super-resolution results of live COS-7 mitochondria labeled by MitoTracker^{TM} Green FM obtained by different methods at two specific time points. a, d Comparison of wide-field images and super-resolution images obtained by FP-SIM, where wide-field images are displayed in the bottom left triangle and super-resolution images are shown on the upper right. The raw SIM images (from our previous work[24], and recorded the mitochondrial dynamic tubulation (MDT) event) with the resolution of 512×512 were captured through a 60× objective (UPlanXApo 60×/1.42 Oil, Olympus, Japan). **b, e** Magnified wide-field image and super-resolution images obtained by PCA-SIM and FP-SIM from the white boxed regions in (**a**) and (**d**). **c, f** Magnified wide-field image and super-resolution images obtained by PCA-SIM and FP-SIM from the yellow boxed regions in (**a**) and (**d**). Yellow arrows point to regions where reconstruction differences are distinct. Scale bars: 5 μm (**a, d**); 1 μm (**b, e, f**); 500 nm (**c**); 3 μm (**d**)

Table S2. Time consumption of FP-SIM for all super-resolution results

No.	Raw image resolution	Time/s	Data source	Sample type
Fig. 2	1024×1024	24.8288±0.1947	Simulation	Complex cell structures
Fig. 3a-3e	1024×1024	24.7055±0.2438	100X/1.4NA	Mitochondria, actin and nucleus of fixed BPAE cells
Fig. 4a-4g	1024×1024	24.6099±0.2775	100X/1.4NA	Mitochondria of fixed BPAE cells
Fig. 5	512×512	6.5159±0.1012	100X/1.4NA	Mitochondria of live COS-7 cells
Fig. S8	1578×1578	68.7213±0.0149	Simulation	Simple standard structures
Fig. S12	1024×1024	24.7575±0.2691	100X/1.4NA	Mitochondria, actin and nucleus of fixed BPAE cells
Fig. S13	1024×1024	24.9992±0.1813	100X/1.45NA	Microtubules of COS-7 cells
Fig. S14a	1024×1024	24.6498±0.3018	N-SIM 100X/1.49NA	Fixed ascaris sample
Fig. S14b	1024×1024	24.6586±0.2709	N-SIM 100X/1.49NA	Actin of fixed BPAE cells
Fig. S17	512×512	6.5159±0.1012	100X/1.4NA	Mitochondria of live COS-7 cells
Fig. S18	512×512	6.5517±0.0836	60X/1.42NA	Mitochondria of live COS-7 cells

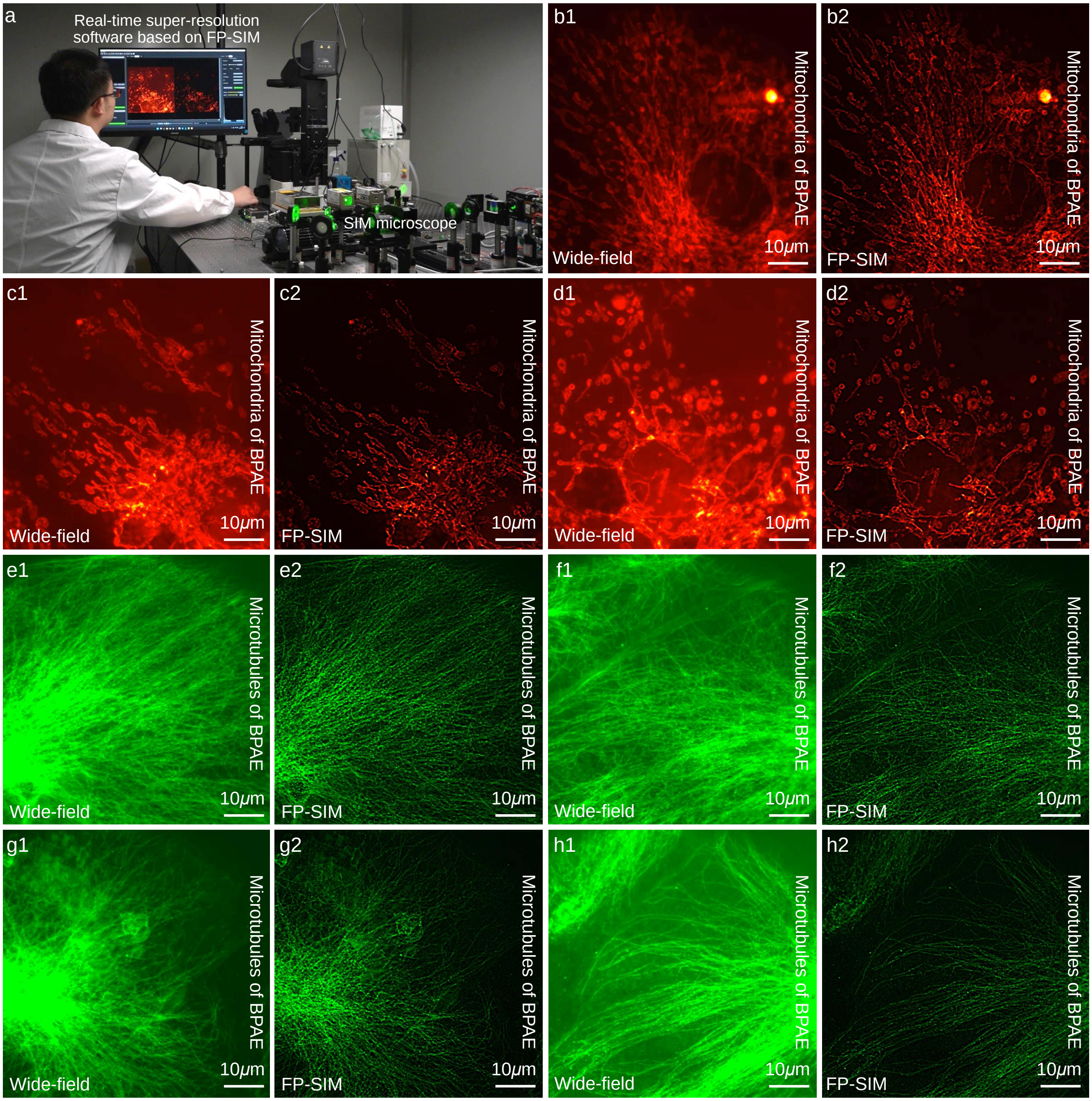

Figure S19. Real-time super-resolution results based on FP-SIM at different time points. a Experimental scenes of real-time super-resolution imaging. **b-d** Wide-field images and super-resolution images obtained by FP-SIM. The raw SIM images (BPAE mitochondria) with a resolution of 1024×1024 were captured through a 100× objective (UPlanXApo 100×/1.45 Oil, Olympus, Japan). **e-h** Wide-field images and super-resolution images obtained by FP-SIM. The raw SIM images (COS-7 microtubules) with a resolution of 1024×1024 were captured through a 100× objective (UPlanXApo 100×/1.45 Oil, Olympus, Japan). See Supplementary Movie S2 for complete super-resolution results. Scale bars: 10 μm (**b-h**)

S12. Supplementary MATLAB code and datasets for FP-SIM

We provide the open-source MATLAB code and associated dataset of FP-SIM, as well as the corresponding user guide.

Overview of FP-SIM MATLAB code and dataset

Supplementary code and dataset contain two subfolds (the "func" folder and the "rawdata" folder), 1 TEXT file (*.txt) and 1 MATLAB file (*.m):

- The MATLAB file "main.m" is the main program that implements FP-SIM, and it contains image preprocessing, illumination pattern extraction, initial target estimation, and iteration steps.
- The folder "func" contains the functions needed to run the MATLAB file "main.m". The main function files include the function "Reserve_Fringe.m" for extracting the illumination pattern, the functions "NortchFilter.m" and "dtft.m" for generating the centre-notched Hanning window, and the functions "SimOtfProvider.m", "otfToVector.m" and "writeOtfVector.m" for generating simulated PSF and OTF. These functions were adapted from HiFi-SIM[14].
- The folder "rawdata" provides the raw SIM images captured by our home-made SIM microscope and other commercial SIM microscopes, and a text file ("para.txt") describing the system parameters of these data:
  - "Ours" folder contains the raw SIM images collected by our home-made SIM microscope through the 100×/1.4NA and 100×/1.44NA objective lenses (UPlanSApo 100×/1.40 Oil, Olympus, Japan; UPlanXApo 100×/1.45 Oil):
    - "Fixed" folder contains four subfolders, which are the raw SIM images of fixed samples:

      In "1" subfolder, image files 405_1.tif, 488_1.tif and 561_1.tif are the raw SIM images (1024×1024 resolution) of a BPAE sample with DAPI-labeled nucleus, Alexa Fluor^{TM} 488-labeled actin and MitoTracker Red^{TM} CMXRos-labeled mitochondria. 405_1.tif are the raw SIM images of the nucleus excited by 405 nm laser, 488_1.tif are the images of actin excited by 488 nm laser, and 561_1.tif are those of mitochondria excited by 561 nm laser. These images are the raw data for Fig. 3 in the main text.

      In "2" subfolder, image files 561_2_25.tif, 561_2_50.tif and 561_2_100.tif are the raw SIM images (1024×1024 resolution) of BPAE mitochondria, which were collected at 100%, 50% and 25% of the excitation power, respectively. These images are the raw data for Fig. 4 in the main text.

      In "3" subfolder, image files 405_3.tif, 488_3.tif and 561_3.tif are another set of the raw SIM images (1024×1024 resolution) of the BPAE sample. These images are the raw data for Fig. S9 in the supplementary information.

    In “4” subfolder, image file 488_4.tif is the raw SIM images (1024×1024 resolution) of COS-7 microtubules labeled by BODIPY^R FL goat anti-mouse IgG. These images were excited by 488 nm laser, and are the raw data for Fig. S10 in the supplementary information.

    - “Live” folder contains the raw SIM images of live cells. In it, image files 561_5_1.tif and 561_5_600.tif are the raw SIM images (512×512 resolution) of live COS-7 mitochondria labeled by MitoTracker^{TM} Green FM obtained at the 1st and 600th time points. These images are the raw data for Fig. 5 in the main text.
    - “Simulation” folder contains the simulated SIM images raw.tif (1024×1024 resolution), which are the raw data for Fig. 1 in the main text.
  - “N-SIM” folder contains the raw SIM images (1024×1024 resolution) collected by N-SIM (Nikon, Japan) through a 100× objective (CFI Apochromat TIRF 100× Oil, NA 1.49, Nikon, Japan). In it, image files raw488.tif and SIM-reconstruction.tif are the original SIM images and the super-resolution image obtained by N-SIM, respectively. The sample is the actin of BPAE cells labeled by Alexa Fluor^{TM} 488. These images are the raw data for Fig. S9 in the supplementary information.

- The file “License.txt” is our copyright notice for the code.

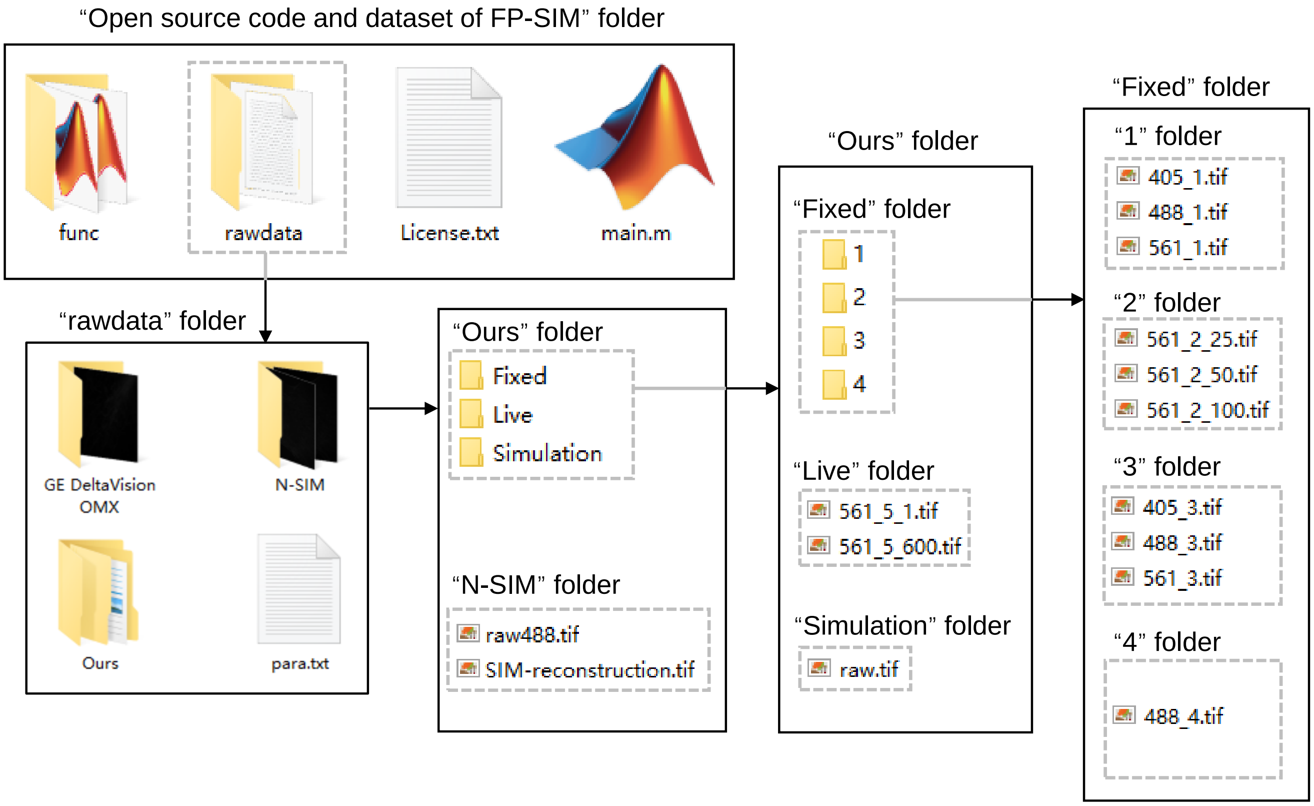

Figure S20. The folder of the open source code and dataset of FP-SIM

User guide for the first test demo

Read raw SIM images

When the demo code ("main.m") is run, first the original SIM images are read and represented by the variable "Raw" (Fig. S21). For generality, the read images are three-step phase-shifting illumination patterns with three different illumination orientations (the subsequent reconstruction requires only three SIM images, one for each orientation). The raw SIM images are then slightly edge-attenuated to prevent edge-related artifacts by the function "importImages".

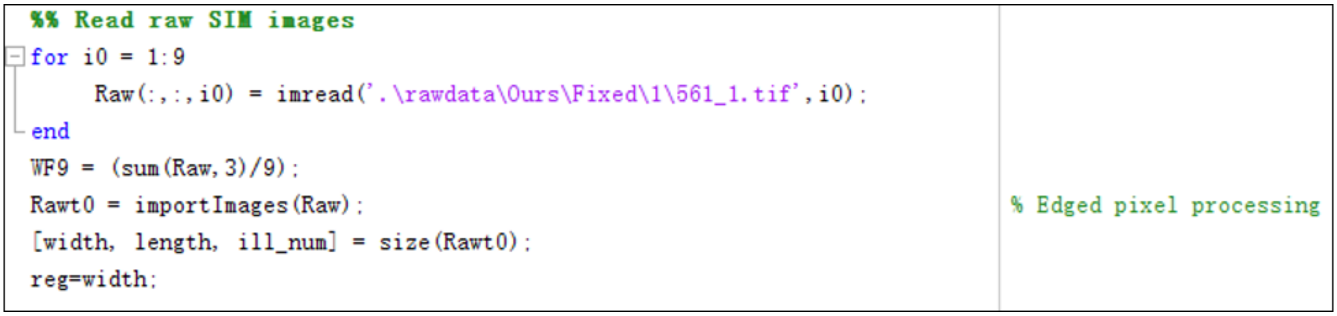

```
%% Read raw SIM images
for i0 = 1:9
     Raw(:,:,i0) = imread('.\rawdata\Ours\Fixed\1\561_1.tif',i0);
end
WF9 = (sum(Raw,3)/9);
Rawt0 = importImages(Raw);                                          % Edged pixel processing
[width, length, ill_num] = size(Rawt0);
reg=width;
```

Figure S21. Code for reading raw SIM images

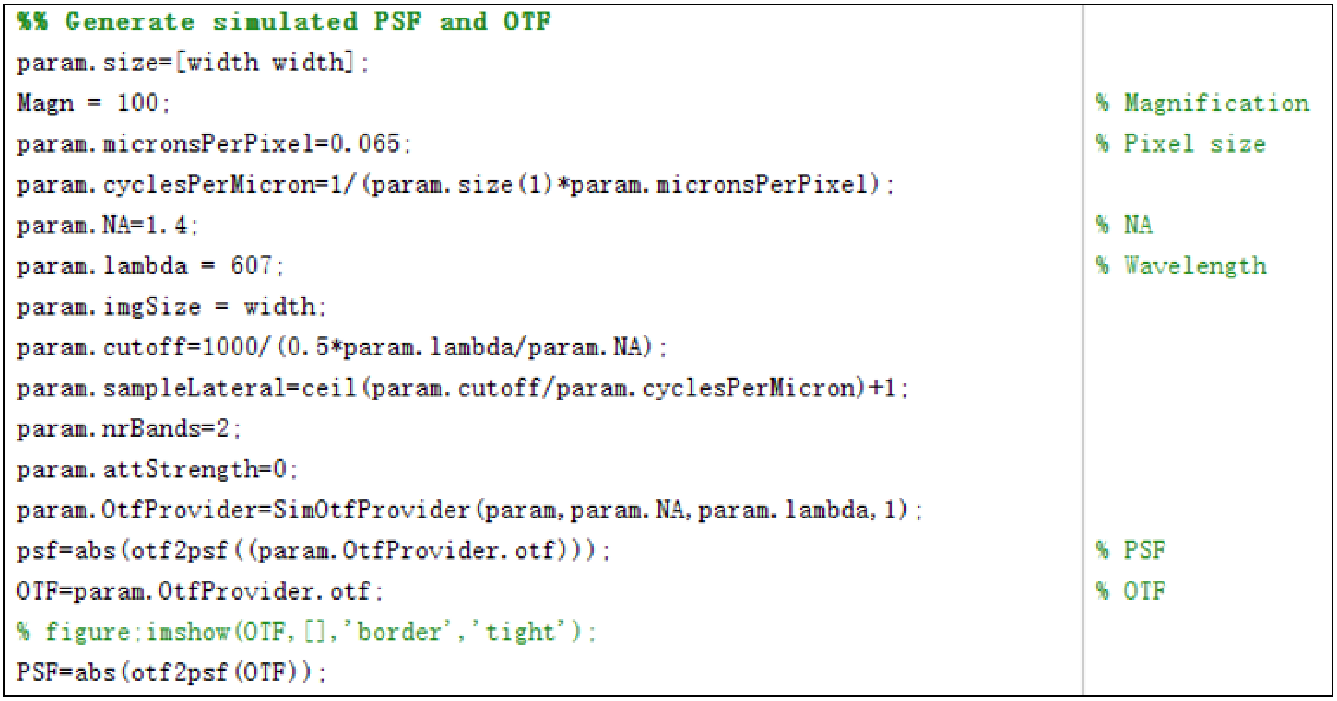

```
%% Generate simulated PSF and OTF
param.size=[width width];
Magn = 100;                                                                % Magnification
param.micronsPerPixel=0.065;                                               % Pixel size
param.cyclesPerMicron=1/(param.size(1)*param.micronsPerPixel);
param.NA=1.4;                                                              % NA
param.lambda = 607;                                                        % Wavelength
param.imgSize = width;
param.cutoff=1000/(0.5*param.lambda/param.NA);
param.sampleLateral=ceil(param.cutoff/param.cyclesPerMicron)+1;
param.nrBands=2;
param.attStrength=0;
param.OtfProvider=SimOtfProvider(param,param.NA,param.lambda,1);
psf=abs(otf2psf((param.OtfProvider.otf)));                                 % PSF
OTF=param.OtfProvider.otf;                                                 % OTF
% figure;imshow(OTF,[],'border','tight');
PSF=abs(otf2psf(OTF));
```

Figure S22. Code for generating PSF and OTF

Generate simulated PSF and OTF

Set system parameters to generate simulated PSF and OTF (Fig. S22). System parameters include objective magnification, objective numerical aperture (NA), camera pixel size and wavelength of the excited fluorescence. Users can change these parameters to suit their system and samples.

Preprocess by RL deconvolution

Then the Richardson-Lucy deconvolution is applied to remove partial Poisson noise and out-of-focus background, while enhancing the peaks of the first-order spectrum for the subsequent illumination pattern extraction (Fig. S23). The preprocessed SIM images are represented by the variable "IIraw".

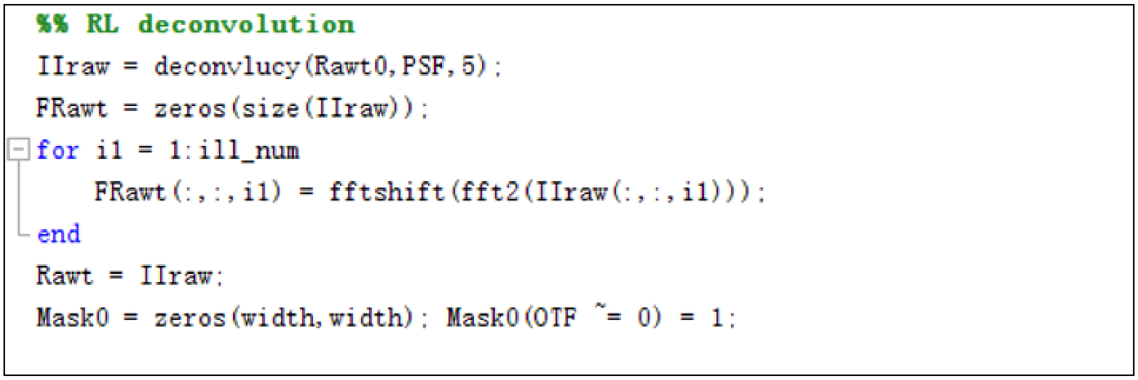

```
%% RL deconvolution
IIraw = deconvlucy(Rawt0,PSF,5);
FRawt = zeros(size(IIraw));
for i1 = 1:ill_num
    FRawt(:,:,i1) = fftshift(fft2(IIraw(:,:,i1)));
end
Rawt = IIraw;
Mask0 = zeros(width,width); Mask0(OTF ~= 0) = 1;
```

Figure S23. **Code for RL deconvolution-based preprocessing**

Illumination pattern extraction

Illumination pattern extraction is achieved by the function "Reserve_Fringe" from the SIM images after preprocessing in the previous step (Fig. S24). Regarding the localization of the integer-pixel peaks of each spectrum component, we directly extract the image center for the 0-order spectrum. Then we use a notch filter (variables "notch_filter1" and "notch_filter2") to eliminate the influence of the 0-order spectrum to locate the peaks of the 1-order spectrums. In the case of very low SNRs or other low illumination pattern modulation, an empirical mask (variable "ex_mask") can also be set based on advance calibration to assist in the peak location (Fig. S25). The extracted illumination patterns are represented by the variable "Friter".

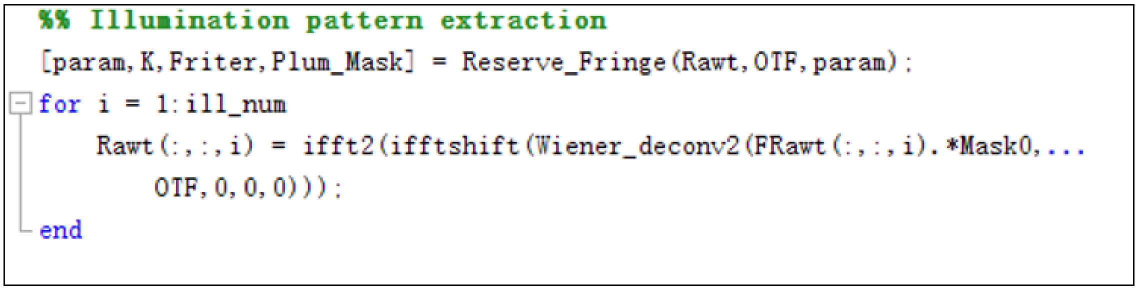

```
%% Illumination pattern extraction
[param,K,Friter,Plum_Mask] = Reserve_Fringe(Rawt,OTF,param);
for i = 1:ill_num
    Rawt(:,:,i) = ifft2(ifftshift(Wiener_deconv2(FRawt(:,:,i).*Mask0,...
        OTF,0,0,0)));
end
```

Figure S24. **Code for illumination pattern extraction**

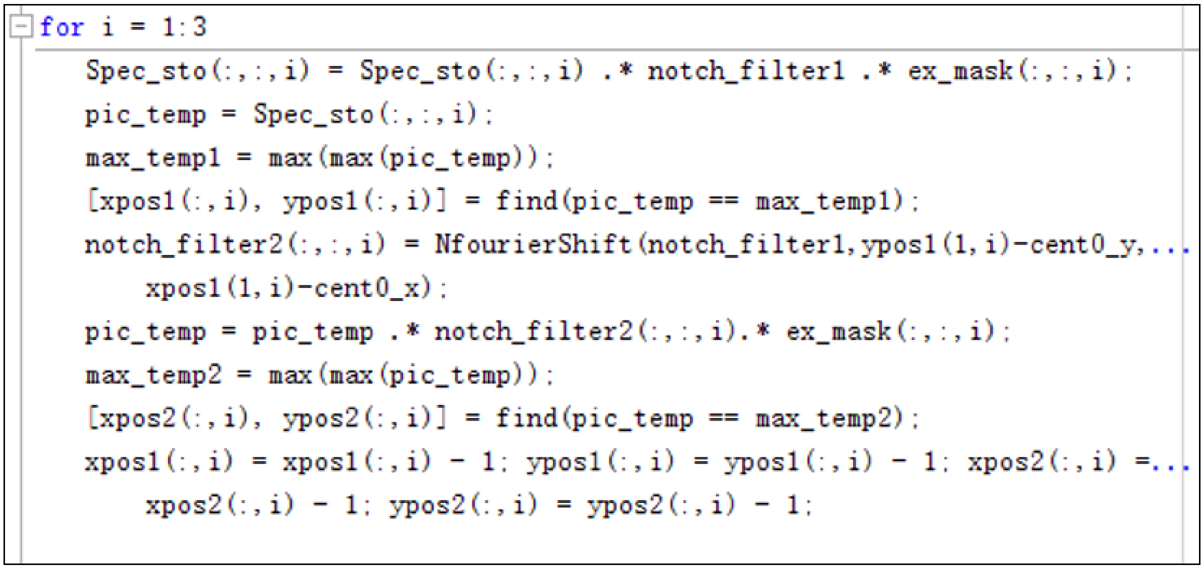

```
for i = 1:3
    Spec_sto(:,:,i) = Spec_sto(:,:,i) .* notch_filter1 .* ex_mask(:,:,i);
    pic_temp = Spec_sto(:,:,i);
    max_temp1 = max(max(pic_temp));
    [xpos1(:,i), ypos1(:,i)] = find(pic_temp == max_temp1);
    notch_filter2(:,:,i) = NfourierShift(notch_filter1,ypos1(1,i)-cent0_y,...
        xpos1(1,i)-cent0_x);
    pic_temp = pic_temp .* notch_filter2(:,:,i).* ex_mask(:,:,i);
    max_temp2 = max(max(pic_temp));
    [xpos2(:,i), ypos2(:,i)] = find(pic_temp == max_temp2);
    xpos1(:,i) = xpos1(:,i) - 1; ypos1(:,i) = ypos1(:,i) - 1; xpos2(:,i) =...
        xpos2(:,i) - 1; ypos2(:,i) = ypos2(:,i) - 1;
```

Figure S25. **Code for the localization of the integer-pixel peaks of 1-order spectrums**

Generate the centre-notched Hanning window

The centre-notched Hanning window is then generated based on the peak distance between the +1-order spectrum and the -1-order spectrum (Fig. S26). The generated filter window is represented by the variable “NotchWin”.

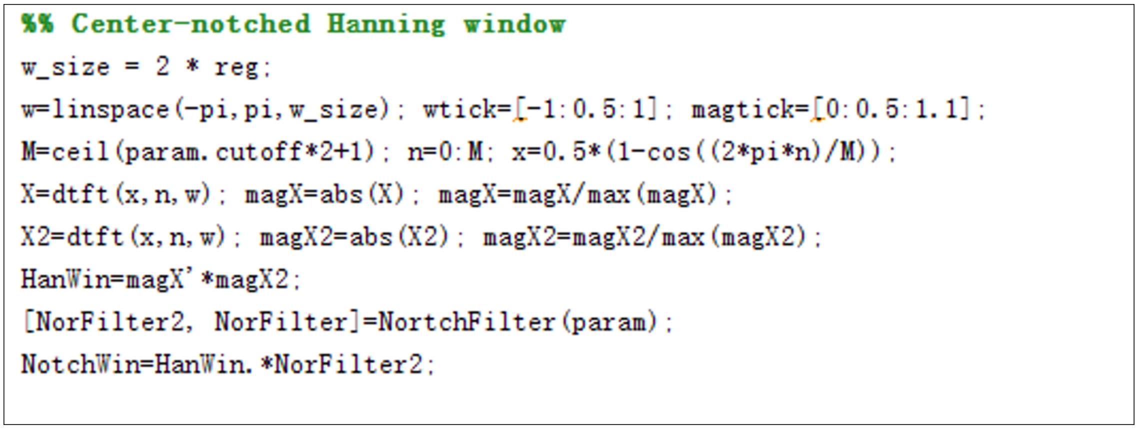

```
%% Center-notched Hanning window
w_size = 2 * reg;
w=linspace(-pi,pi,w_size); wtick=[-1:0.5:1]; magtick=[0:0.5:1.1];
M=ceil(param.cutoff*2+1); n=0:M; x=0.5*(1-cos((2*pi*n)/M));
X=dtft(x,n,w); magX=abs(X); magX=magX/max(magX);
X2=dtft(x,n,w); magX2=abs(X2); magX2=magX2/max(magX2);
HanWin=magX'*magX2;
[NorFilter2, NorFilter]=NortchFilter(param);
NotchWin=HanWin.*NorFilter2;
```

Figure S26. **Code for generating the centre-notched Hanning window**

Estimate the initial image

Before the initial estimation, the SIM images and the extracted illumination images are first doubled in size to create sufficient sampling rate for the subsequent super-resolution. The SIM images and the illumination patterns of two times the size are represented by the variables “IRaw” and “Frit”. Then the initial super-resolution image is acquired directly from one SIM image using the centre-notched Hanning window “NotchWin” obtained in the previous step (Fig. S27). The initial estimate is represented by the variable “Iobj”.

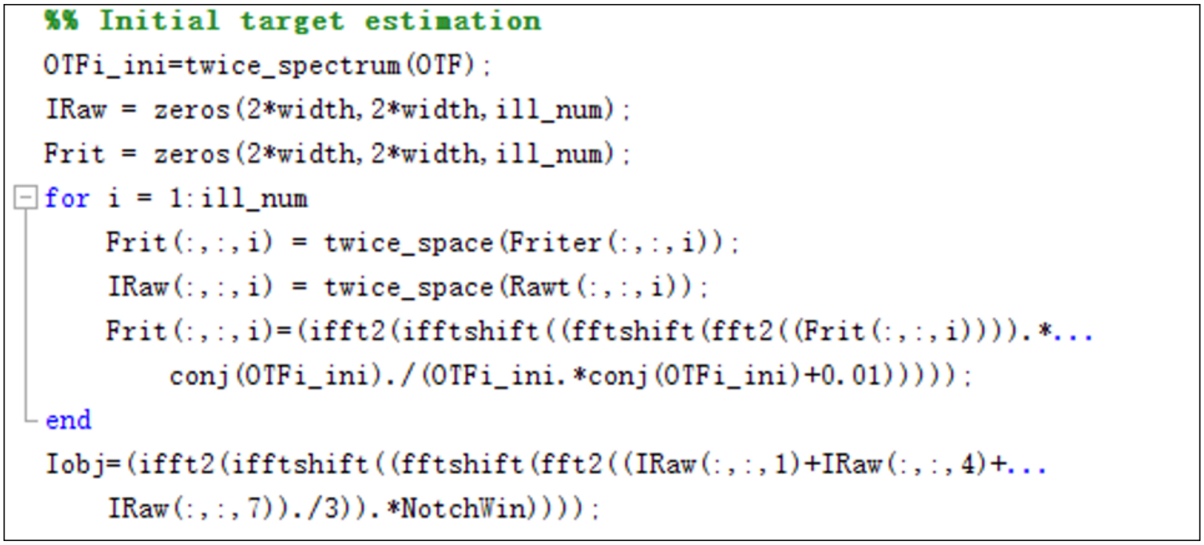

```
%% Initial target estimation
OTFi_ini=twice_spectrum(OTF);
IRaw = zeros(2*width,2*width,ill_num);
Frit = zeros(2*width,2*width,ill_num);
for i = 1:ill_num
    Frit(:,:,i) = twice_space(Friter(:,:,i));
    IRaw(:,:,i) = twice_space(Rawt(:,:,i));
    Frit(:,:,i)=(ifft2(ifftshift((fftshift(fft2((Frit(:,:,i)))).*...
        conj(OTFi_ini)./(OTFi_ini.*conj(OTFi_ini)+0.01)))));
end
Iobj=(ifft2(ifftshift((fftshift(fft2((IRaw(:,:,1)+IRaw(:,:,4)+...
    IRaw(:,:,7))./3)).*NotchWin))));
```

Figure S27. **Code for obtaining an initial estimate of the super-resolved image**

Iteration to reconstruct the super-resolution image

Finally, the initial estimate (“Iobj”), the illumination pattern (“Frit”) and the preprocessed SIM images (“IRaw”) acquired by the above steps are used together for iteration (Fig. S28). Note that only one image per illumination orientation (three images in total) is used for the iteration. The variable “Plum_Mask” is the regularization term to limit the target spectrum and ensure convergence. The variable “loop_num” is used to set the iteration times. With each iteration, the updated super-resolution image and the corresponding spectrum map are displayed (Fig. S29). The user can visually observe the changes in spectrum and the resolution. Figure S30 shows the comparison of the final iterative super-resolution result and the wide-field image.

```
%% Iteration
loop_num = 20;                                                % Number of iteration cycles
for i5 = 1:loop_num
        deI1=IRaw(:,:,1)./Frit(:,:,1)-(ifft2(ifftshift(OTFi0.*fftshift...
            (fft2(Iobj)))));
        deI2=IRaw(:,:,4)./Frit(:,:,4)-(ifft2(ifftshift(OTFi0.*fftshift...
            (fft2(Iobj)))));
        deI3=IRaw(:,:,7)./Frit(:,:,7)-(ifft2(ifftshift(OTFi0.*fftshift...
            (fft2(Iobj)))));
        FdeI1=fftshift(fft2(deI1));
        FdeI2=fftshift(fft2(deI2));
        FdeI3=fftshift(fft2(deI3));
        fftWiener=(ifft2(fftshift(((FdeI1.*conj(OTFi0)+FdeI2.*...
            conj(OTFi0)+FdeI3.*conj(OTFi0))./(OTFi0.*conj(OTFi0)+0.1)))));
        Iobj=Iobj+fftWiener;
        Iobj(Iobj < 0) = 0;
spec=fftshift(fft2(Iobj));
spec = spec.*Plum_Mask;
Iobj = (ifft2(ifftshift(spec)));
subplot(121);imshow(Iobj,[]);title('Updated target');
subplot(122);imshow(log(abs(spec)+1),[]);title(['Loop Num=',num2str(i5)]);
pause(0.000025);
end

Iobj=abs(Iobj);
   Iobj = (Iobj) - min(min((Iobj)));
```

Figure S28. Code for iteratively acquiring the super-resolution image

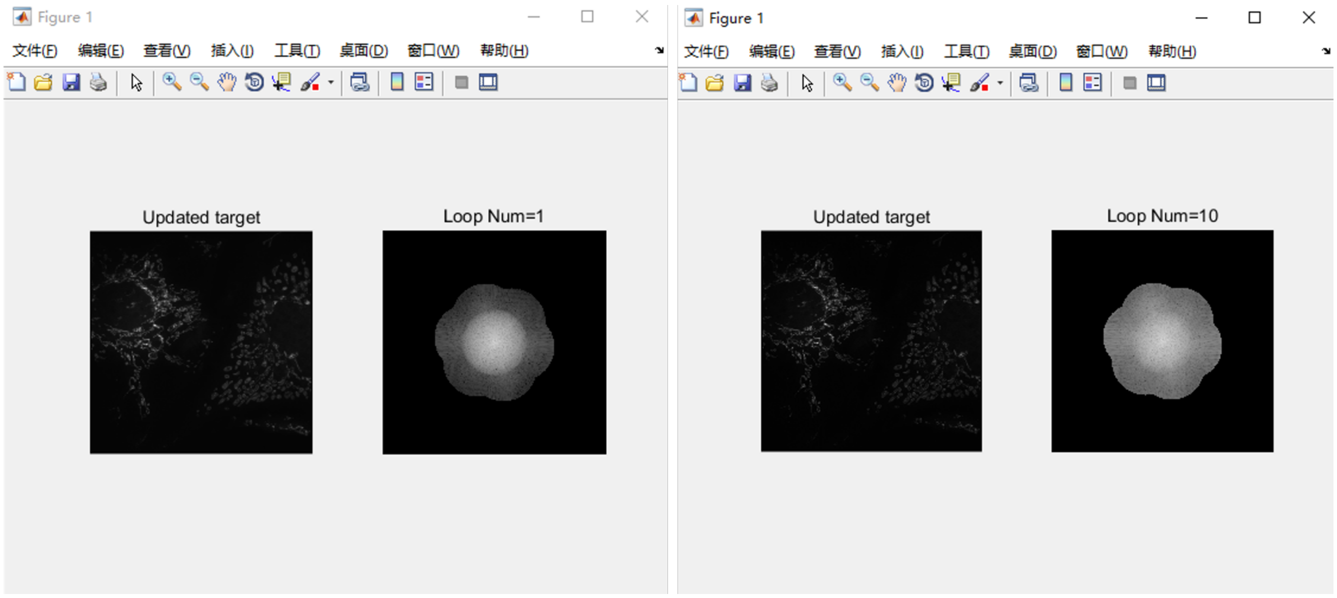

Figure S29. The results of 1 iteration and 10 iterations

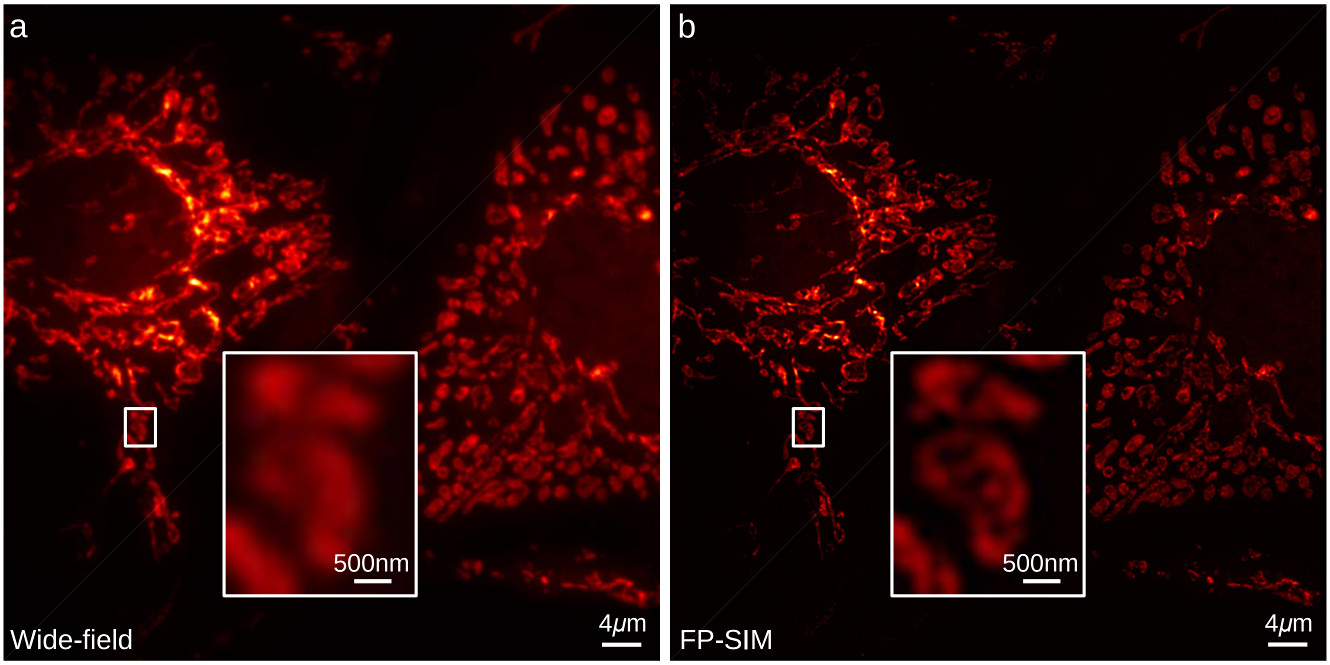

Figure S30. **Comparison of the final iterative super-resolution result and the wide-field image. a** Wide-field image. **b** Super-resolution image obtained by FP-SIM

References

1. Gustafsson, M. G. Surpassing the lateral resolution limit by a factor of two using structured illumination microscopy. *J. Microsc.* **198**, 82–87 (2000).

2. Huang, X. *et al.* Fast, long-term, super-resolution imaging with hessian structured illumination microscopy. *Nat. Biotechnol.* **36**, 451–459 (2018).

3. Gustafsson, M. G. *et al.* Three-dimensional resolution doubling in wide-field fluorescence microscopy by structured illumination. *Biophys. J.* **94**, 4957–4970 (2008).

4. Zheng, G., Horstmeyer, R. & Yang, C. Wide-field, high-resolution fourier ptychographic microscopy. *Nat. Photonics* **7**, 739–745 (2013).

5. Snyder, D. L., Hammoud, A. M. & White, R. L. Image recovery from data acquired with a charge-coupled-device camera. *J. Opt. Soc. Am. A* **10**, 1014–1023 (1993).

6. Mudry, E. *et al.* Structured illumination microscopy using unknown speckle patterns. *Nat. Photonics* **6**, 312–315 (2012).

7. Dupé, F.-X., Fadili, M.-J. & Starch, J.-L. Inverse problems with poisson noise: Primal and primal-dual splitting. In *2011 18th IEEE International Conference on Image Processing*, 1901–1904 (IEEE, 2011).

8. Lukeš, T. *et al.* Three-dimensional super-resolution structured illumination microscopy with maximum a posteriori probability image estimation. *Opt. Express* **22**, 29805–29817 (2014).

9. Chu, K. *et al.* Image reconstruction for structured-illumination microscopy with low signal level. *Opt. Express* **22**, 8687–8702 (2014).

10. Sun, J., Chen, Q., Zhang, Y. & Zuo, C. Sampling criteria for fourier ptychographic microscopy in object space and frequency space. *Opt. Express* **24**, 15765–15781 (2016).

11. Zuo, C., Sun, J. & Chen, Q. Adaptive step-size strategy for noise-robust fourier ptychographic microscopy. *Opt. Express* **24**, 20724–20744 (2016).

12. Ströhl, F. & Kaminski, C. F. Speed limits of structured illumination microscopy. *Opt. Lett.* **42**, 2511–2514 (2017).

13. Perez, V., Chang, B.-J. & Stelzer, E. H. K. Optimal 2d-sim reconstruction by two filtering steps with richardson-lucy deconvolution. *Sci. Reports* **6**, 1–11 (2016).

14. Wen, G. *et al.* High-fidelity structured illumination microscopy by point-spread-function engineering. *Light. Sci. & Appl.* **10**, 1–12 (2021).

15. Dong, S. *et al.* Resolution doubling with a reduced number of image acquisitions. *Biomed. Opt. Express* **6**, 2946–2952 (2015).

16. Qian, J. *et al.* Robust frame-reduced structured illumination microscopy with accelerated correlation-enabled parameter estimation. *Appl. Phys. Lett.* **121**, 153701 (2022).

17. Zheng, X. *et al.* Acceleration of laser scanning structured illumination microscopy using frame-reduction algorithm. *Available at SSRN 4765395* .

18. Orieux, F., Sepulveda, E., Loriette, V., Dubertret, B. & Olivo-Marin, J.-C. Bayesian estimation for optimized structured illumination microscopy. *IEEE Transactions on Image Process.* **21**, 601–614 (2011).

19. Lal, A. *et al.* A frequency domain sim reconstruction algorithm using reduced number of images. *IEEE Transactions on Image Process.* **27**, 4555–4570 (2018).

20. Zhao, W. *et al.* Quantitatively mapping local quality of super-resolution microscopy by rolling fourier ring correlation. *Light. Sci. & Appl.* **12**, 298 (2023).

21. Qiao, C. *et al.* Evaluation and development of deep neural networks for image super-resolution in optical microscopy. *Nat. Methods* **18**, 194–202 (2021).

22. Wen, G. *et al.* Spectrum-optimized direct image reconstruction of super-resolution structured illumination microscopy. *PhotoniX* **4**, 19 (2023).

23. Zhao, W. *et al.* Sparse deconvolution improves the resolution of live-cell super-resolution fluorescence microscopy. *Nat. Biotechnol.* **40**, 606–617 (2022).

24. Qian, J. *et al.* Structured illumination microscopy based on principal component analysis. *eLight* **3**, 1–13 (2023).